SANDIA REPORT

SAND2016-9631
Unlimited Release
October, 2016

High Fidelity Modeling of Ionic Conduction in Solids

F. P. Doty, X. W. Zhou, P. Yang, M. E. Foster, and H. Fan

Prepared by
Sandia National Laboratories
Albuquerque, New Mexico 87185 and Livermore, California 94550

Sandia National Laboratories is a multi-mission laboratory managed and operated by Sandia Corporation, a wholly owned subsidiary of Lockheed Martin Corporation, for the U.S. Department of Energy's National Nuclear Security Administration under contract DE-AC04-94AL85000.

Sandia National Laboratories

Issued by Sandia National Laboratories, operated for the United States Department of Energy by Sandia Corporation.

Available to DOE and DOE contractors from
U.S. Department of Energy
Office of Scientific and Technical Information
P.O. Box 62
Oak Ridge, TN 37831

Telephone: (865) 576-8401
Facsimile: (865) 576-5728
E-Mail: reports@osti.gov
Online ordering: http://www.osti.gov/scitech

Available to the public from
U.S. Department of Commerce
National Technical Information Service
5301 Shawnee Rd
Alexandria, VA 22312

Telephone: (800) 553-6847
Facsimile: (703) 605-6900
E-Mail: orders@ntis.gov
Online order: http://www.ntis.gov/search

SAND2016-9631
Unlimited Release
October, 2016

High Fidelity Modeling of Ionic Conduction in Solids

F. P. Doty
Radiation and Nuclear Detection Materials and Analysis Department
Livermore, CA 94551-0969

X. W. Zhou
Mechanics of Materials Department
Livermore, CA 94551-0969

M. E. Foster
Materials Chemistry Department
Livermore, CA 94551-0969

P. Yang
Electronic, Optical, and Nano Department
Albuquerque, New Mexico 87185-MS0958

H. Fan
Advanced Materials Laboratory Department
Albuquerque, New Mexico 87185-MS1349

Sandia National Laboratories

Abstract

TlBr has the properties to become the leading radiation detection semiconductor. It has not yet been deployed due to a short lifetime of only hours to weeks. While the rapid structural deteriorations must come from ionic conduction under operating electrical fields, detailed aging mechanisms have not been understood. As a result, progress to extend lifetime has been limited despite extensive studies in the past. We have developed new atomistic simulation capabilities to enable study of ionic conduction under electrical fields. Our combined simulations and experiments indicate that dislocations in TlBr climb under electrical fields. This climb is the root cause for structural deterioration. Hence, we discovered new strengthening methods to reduce aging. Our new atomistic simulation approach can have broader impact on other Sandia programs including battery research. Our project results in 4 publications, a new invention, new LAMMPS capabilities, solution to mission relevant materials, and numerous presentations.

ACKNOWLEDGMENTS

We greatly appreciate Albert A. Talin, Mark A. Rodriguez, Khalid Hatter, Binsong Li from Sandia National Laboratories for helpful discussions and assistance in various experiments including X-ray Rocking curve measurement: ion implantation, and synchrotron measurement. We also thank Len Cirignano from RMD for providing TlBr crystals and the related characterization data.

CONTENTS

FIGURES

TABLES

NOMENCLATURE

di	dimer
dc	diamond-cubic
sc	simple-cubic
bcc	body-centered-cubic
fcc	face-centered-cubic
hcp	hexagonal-closely-packed
zb	zinc-blende
wz	wurtzite
B1	NaCl
B2	CsCl

1. INTRODUCTION

The high cost of the radiation detecting CdZnTe (CZT) crystals has been the main reason as why radiation detection technologies cannot be widely deployed (e.g., on every traffic light). The low cost TlBr has the desired properties for radiation detection including a large band gap (2.7eV), a long carrier lifetime (up to 10^{-4} s), a high average atomic number, and a high resistivity ($\sim 10^{11}$ Ω cm at 298K). As a result, TlBr has demonstrated outstanding performance for room temperature γ-ray detection, reaching resolution ≤ 1% at 662 keV [1,2,3,4,5]. This suggests that TlBr can potentially surpass CZT to become the leading semiconductor for radiation detection. To collect the charges created during the radiation events, the material must be subject to an external electric field. Unfortunately, the performance of TlBr degrades under external electric fields after operation times as short as a few hours to a few weeks [2,6,7,8,9,10,11,12]. As a result, the transition from CZT to TlBr has not occurred.

Enormous efforts have been made in the past to extend the lifetimes of TlBr, including using thallium contacts [7], cooling the detectors [13,14], employing various surface treatments [15,16] , ultra-purification [4], engineered device geometry [17], and making larger crystals [18]. Yet, no technique has been able to solve the rapid degradation problem completely. These previous approaches, however, have not considered intrinsic material defects that are always present, such as dislocations.

Ionic migration of vacancies has been traditionally believed to be the root cause for property degradation. Interestingly, quantum mechanical studies [19,20,21] indicated that to account for the rapid aging of TlBr using the vacancy migration mechanism, the vacancy concentration must be many orders of magnitude higher than any conventional estimates.

The purpose of this project is to develop new computational capability to enable study of ionic migration under external electrical fields when materials have dislocations. We will then use this new capability, coupled with experiments, to study the aging mechanisms of TlBr. Successful methods will make broad impacts on Sandia programs including battery research.

In the following, Chapter 2 develops a TlBr interatomic potential (which has been published as a journal article [22]), Chapter 3 develops an analytical variable charge model (which has been published [23]), Chapter 4 describes our molecular dynamics simulations that lead to the discovery of an extraordinary dislocation-induced aging mechanism, Chapter 5 describes our molecular dynamics "development" of aging-resistant TlBr, and Chapter 6 describes an invention disclosure regarding new methods to synthesis aging-resistant TlBr crystals.

This page is intentionally left blank.

2. A MODIFIED STILLINGER-WEBER POTENTIAL FOR TLBR, AND ITS POLYMORPHIC EXTENSION

I. Abstract

This Chapter has been published [22], and has received positive feedbacks from research committee. To enable molecular dynamics (MD) simulations of TlBr under an operating electrical field, we have developed a Stillinger-Weber type of TlBr interatomic potential. During this process, we have also addressed two problems of wider interests. First, the conventional Stillinger-Weber potential format is only applicable for tetrahedral structures (e.g., diamond-cubic, zinc-blende, or wurtzite). Here we have modified the analytical functions of the Stillinger-Weber potential so that it can now be used for other crystal structures. Second, past modifications of interatomic potentials cannot always be applied by a broad community because any new analytical functions of the potential would require corresponding changes in the molecular dynamics codes. Here we have developed a polymorphic potential model that simultaneously incorporates Stillinger-Weber, Tersoff, embedded-atom method, and any variations (i.e., modified functions) of these potentials. As a result, future modifications of these potentials will no longer require modification of MD codes. We have implemented released this polymorphic model in MD code LAMMPS [24], and demonstrated that our TlBr potential enables stable MD simulations under external electric fields.

II. Introduction

As ionic conduction may be affected by defective structures such as the open channels of edge dislocations, molecular dynamics (MD) that allows extended defects to be included in simulated crystals becomes a useful method to study the ionic conduction induced structural aging of TlBr. Such MD simulations are not yet possible due to the lack of an interatomic potential for the Tl-Br system that has a CsCl type of crystal structure. In addition, past MD simulations [25,26,27,28, 29,30,31,32] mainly focused on ionic conductivity, but not the structural evolution under external electric fields. As a result, these studies typically do not apply external electric fields. Instead, the system is simply annealed at a sufficiently high temperature to cause thermally activated diffusion of ions. The trajectories of ions are then used to calculate diffusion coefficients of ions. These diffusion coefficients are in turn used to calculate ionic conductivity through Nernst-Einstein relation. Our interest is to understand the structural evolution under external electric fields. Hence, we will apply an external electric field to accelerate the ionic motion, therefore leading to sufficient structural changes needed for the analysis within the short time scale of MD simulations. This, however, requires a robust interatomic potential that can at least maintain the crystal structure at a large external field.

While relatively complex many-body potential [33] can be applied, it is not uncommon to model ionic materials with simple force fields such as pair potentials [25-28], or pair potentials plus angular energy penalty interactions [29,30]. The angular energy penalty approach is very similar to the widely-used Stillinger-Weber (SW) potential [34], and has the advantage to stabilize relatively complex crystal structures that the pair potentials cannot. For example, SW potentials use a parabolic energy penalty term to penalize non-tetrahedral bond angles. As a result, SW potentials have been successfully applied to tetrahedral structures such as diamond-cubic, zinc-

blende, and wurtzite. Depending on parameterization, SW potentials can also be used for fcc elements [35,36,37]. However, the conventional SW potentials have two limitations [34,35,36]: (1) they significantly overestimate the elastic constants of closely packed (e.g., fcc) elements; and (2) they usually cannot be used for other (non-tetrahedral) structures such as sc elements, and NaCl and CsCl compounds. Note that although most elements do not exhibit the lowest energy for the sc crystal, the sc crystal can have a near-lowest energy that cannot be captured by SW potentials. Potentials capable of prescribing a low energy for the sc structure, therefore, improve upon SW potentials in terms of the general energy trends when a variety of configurations are considered [38].

Many literature potentials are constructed using particular analytical functions. These potentials can be easily improved if alternative functions are used. For example, Rockett [39] used alternative functions in the Tersoff [40,41] potential format to better treat short- and long- range interactions in covalent systems, and we used alternative functions in the Tersoff potential to improve its prediction on thermal conductivity [42]. Although alternative functions do not change the potential format and should, therefore, be easily applied, such an approach has not been widely used because it does require new molecular dynamics codes to be developed for each modified function.

With the recognition that the problems described above can limit the atomistic level studies of emerging important materials, the objective of the present Chapter is fourfold: (1) modify the SW potential so that it can better describe elastic constants of elements and be applicable to a wide range of crystal structures including sc, NaCl, and CsCl; (2) develop a polymorphic potential model that incorporates simultaneously SW potential, modified SW potential, Tersoff potential [39,40], modified Tersoff potential [38], and embedded-atom method (EAM) potential [43] ; (3) implement this polymorphic potential model in the public MD code LAMMPS [22] so that future development of any alternative functions for these types of potentials no longer requires modification of the molecular dynamics codes; and (4) parameterize the modified SW potential for TlBr system and demonstrate the utility of the resulting potential under external electric fields.

III. ***Modified Potential***

In SW potential [33], the total energy of a system of N atoms is expressed as

$$E = \frac{1}{2}\sum_{i=1}^{N}\sum_{j=i_1}^{i_N}\left[\phi_{R,IJ}(r_{ij}) - \phi_{A,IJ}(r_{ij}) + u_{IJ}(r_{ij})\sum_{\substack{k=i_1 \\ k\neq j}}^{i_N} u_{IK}(r_{ik})\cdot g_{JIK}(\cos\theta_{jik})^2\right] \quad (1)$$

where i_1, i_2, …, i_N is a list of neighbors of atom i, θ_{jik} is the bond angle formed by atoms j and k at the site of atom i, $\phi_{R,IJ}(r_{ij})$ and $\phi_{A,IJ}(r_{ij})$ are, respectively, pairwise repulsive and attractive functions, $u_{IJ}(r_{ij})$ is another pair function for the three-body term, $g_{JIK}(\cos\theta_{jik})$ is an angular energy penalty function, and subscripts i,j,k and I,J,K indicate, respectively, the atoms and the species of the atoms (note that three bodies JIK and KIJ are equivalent). The original SW potentials significantly overestimate the elastic constants of elements because the $\phi_{R,IJ}(r)$ and $\phi_{A,IJ}(r)$ functions used in these potentials do not allow independent adjustment of bond energy and its second derivative [34]. Here we propose to use modified Morse's functions capable of

independent change of bond energy and its second derivative [34] to represent $\phi_{R,IJ}(r)$ and $\phi_{A,IJ}(r)$:

$$\phi_{R,IJ}(r) = \frac{E_{b,IJ} \cdot \beta_{IJ}}{\beta_{IJ} - \alpha_{IJ}} \cdot \exp\left(-\alpha_{IJ} \cdot \frac{r - r_{0,IJ}}{r_{0,IJ}} \right) \cdot f_{c,IJ}(r), \tag{2}$$

$$\phi_{A,IJ}(r) = \frac{E_{b,IJ} \cdot \alpha_{IJ}}{\beta_{IJ} - \alpha_{IJ}} \cdot \exp\left(-\beta_{IJ} \cdot \frac{r - r_{0,IJ}}{r_{0,IJ}} \right) \cdot f_{c,IJ}(r), \tag{3}$$

where $E_{b,IJ}$, $r_{0,IJ}$, α_{IJ}, and β_{IJ} are four pair dependent parameters, and $f_{c,IJ}(r_{ij})$ is a cutoff function. Note that the parameters introduced here have physical meanings: $E_{b,IJ}$ and $r_{0,IJ}$ correspond respectively to the equilibrium bond energy and bond length, and $\alpha_{IJ} >> \beta_{IJ}$ control the curvature of the bond energy at the equilibrium bond length. The cutoff function $f_{c,IJ}(r_{ij})$ is expressed as:

$$f_{c,IJ}(r) = \begin{cases} \dfrac{\exp\left(-\varsigma_{IJ} \cdot r^{\upsilon_{IJ}}\right) - \exp\left(-\varsigma_{IJ} \cdot r_{c,IJ}^{\upsilon_{IJ}}\right)}{\exp\left(-\varsigma_{IJ} \cdot r_{s,IJ}^{\upsilon_{IJ}}\right) - \exp\left(-\varsigma_{IJ} \cdot r_{c,IJ}^{\upsilon_{IJ}}\right)}, & r \le r_{c,IJ} \\ 0, & r > r_{c,IJ} \end{cases} \tag{4}$$

where $r_{s,IJ}$ and $r_{c,IJ}$ ($r_{s,IJ} << r_{c,IJ}$) are two independent pair parameters, and ς_{IJ} and υ_{IJ} are two dependent pair parameters $\upsilon_{IJ} = \dfrac{\ln\left[\ln(0.9)/\ln(0.00000001)\right]}{\ln\left(r_{s,IJ}/r_{c,IJ}\right)}$ and $\varsigma_{IJ} = -\dfrac{\ln(0.9)}{\left(r_{s,IJ}\right)^{\upsilon_{IJ}}}$. Note that the cutoff function approximately equals one at $r \le r_{s,IJ}$ and equals zero at $r = r_{c,IJ}$ (i.e., $r_{c,IJ}$ is the cutoff distance). Hence, multiplying any potential function with this cutoff function does not affect significantly the potential function at small distances but allows the potential function to be smoothly cut off at $r_{c,IJ}$. Such a cutoff method is superior to the spline approach used by the Tersoff potential as the latter does not have continuous second and higher order derivatives. A general exponential decay function is used to represent the $u_{IJ}(r)$ function:

$$u_{IJ}(r) = \exp\left(-\gamma_{IJ} \cdot \frac{r_{ij} - r_{0,IJ}}{r_{0,IJ}} \right) \cdot f_{c,IJ}(r_{ij}) \tag{5}$$

where γ_{IJ} is a pair parameter.

For the angular function, SW potentials use a parabolic energy penalty to the non-tetrahedral angle $g_{JIK}(\cos\theta_{jik}) = (\cos\theta_{jik} - \cos\theta_{0,JIK})^2$ where the parameter $\cos\theta_{0,JIK}$ is fixed at the tetrahedral bond angle $\cos\theta_{0,JIK} = -1/3$. This imposes two constraints: not only the favorable bond angle is fixed at the tetrahedral angle, but also the favorable bond angle does not depend on species I, J, and K. The $g_{JIK}(\cos\theta_{jik})$ function can be made more general by treating $\cos\theta_{0,JIK}$ as fitting parameters that depend on I, J, and K. Even so, the resulting function is still not fully flexible, for instance, it does not have a scaling factor, and its second derivative with respect to $\cos\theta_{jik}$ is fixed at 2. In addition, the function is symmetric at $\cos\theta_{jik} = \cos\theta_{0,JIK}$, and the energy penalty does not saturate (i.e., the absolute slope increases when the angle deviates from $\cos\theta_{0,JIK}$). These cause difficulties for capturing the angular function derived from quantum mechanical theories [44] . Here we consider a new angular function $g_{JIK}(\cos\theta_{jik}) = \lambda_{JIK} \cdot \{1 - \exp[-\xi_{0,JIK} \cdot (\cos\theta_{jik} - \cos\theta_{0,JIK})^2]\}$, where λ_{JIK} is three-body dependent scaling factor and $\xi_{0,JIK}$ is another three-body dependent parameter. Note that for $\lambda_{JIK} = 1$, $\xi_{0,JIK} = 1$ and $\cos\theta_{0,JIK} = -1/3$, the modified energy penalty is equivalent to the parabolic function near $\cos\theta_{jik} = -1/3$ because the first term of the Taylor series of the modified function expanded at $\cos\theta_{jik} = \cos\theta_{0,JIK}$ is in fact the parabolic

function. However, replacing the leading term with a full series does allow the energy penalty curvature to be adjusted through an added parameter $\xi_{0,JIK}$ and the value of function to be saturated (while retaining the "penalty" effect, i.e., the function minimizes at $\cos\theta_{jik} = \cos\theta_{0,JIK}$ and monotonically increases when $\cos\theta_{jik}$ deviates from $\cos\theta_{0,JIK}$). An even further flexible function will be to penalize the energy when the bond angle deviates from three independent values, which also results in asymmetric minimums. Based on this consideration, we propose a general angular function as:

$$g_{JIK}(\cos\theta_{jik}) = \lambda_{JIK} \cdot \frac{1-\exp\left[-\xi_{0,JIK}\cdot(\cos\theta_{jik}-\cos\theta_{0,JIK})^2\right]}{1-\exp\left[-\xi_{0,JIK}\cdot(1-\cos\theta_{0,JIK})^2\right]} \cdot \frac{1-\kappa_{1,JIK}\cdot\exp\left[-\xi_{1,JIK}\cdot(\cos\theta_{jik}-\cos\theta_{1,JIK})^2\right]}{1-\kappa_{1,JIK}\cdot\exp\left[-\xi_{1,JIK}\cdot(1-\cos\theta_{1,JIK})^2\right]} \cdot \frac{1-\kappa_{2,JIK}\cdot\exp\left[-\xi_{2,JIK}\cdot(\cos\theta_{jik}-\cos\theta_{2,JIK})^2\right]}{1-\kappa_{2,JIK}\cdot\exp\left[-\xi_{2,JIK}\cdot(1-\cos\theta_{2,JIK})^2\right]} \tag{6}$$

where λ_{JIK}, $\xi_{0,JIK}$, $\xi_{1,JIK}$, $\xi_{2,JIK}$, $\cos\theta_{0,JIK}$, $\cos\theta_{1,JIK}$, $\cos\theta_{2,JIK}$, $\kappa_{1,JIK}$, and $\kappa_{2,JIK}$ are all three-body dependent parameters. Note that when the parameters are given, the denominator in Eq. (6) is essentially a normalization constant so that $g_{JIK}(\cos\theta_{jik}=1) = \lambda_{JIK}$. It can be seen that when $\kappa_{1,JIK} = \kappa_{2,JIK} = 0$, Eq. (6) penalizes the energy when the bond angle deviates from a single value $\cos\theta_{jik} = \cos\theta_{0,JIK}$ as in the conventional SW potential. Otherwise Eq. (6) can penalize the energy when the bond angle deviates from three values $\cos\theta_{jik} = \cos\theta_{0,JIK}$, $\cos\theta_{jik} = \cos\theta_{1,JIK}$, $\cos\theta_{jik} = \cos\theta_{2,JIK}$. Eqs. (1) – (6) fully define our modified SW (MSW) potential.

IV. ***Polymorphic Potential Model***

Any improved interatomic potentials will not be applied unless molecular dynamics codes are available to run them. To provide potential developers with a great flexibility for modifying the interatomic potentials without worrying about MD codes, we have constructed a polymorphic potential model. In this model, the energy of the system is expressed as

$$E = \frac{1}{2}\sum_{i=1}^{N}\sum_{j=1}^{N}\left[(1-\delta_{ij})\,U_{IJ}(r_{ij}) + (1-\eta_{ij})\,F_{IJ}(X_{ij})\,V_{IJ}(r_{ij})\right] \tag{7}$$

where δ_{ij} is Kronecker delta (i.e., $\delta_{ij} = 1$ when $i = j$ and $\delta_{ij} = 0$ when $i \neq j$), η_{ij} is an indicator of the potential type that can be set to either $\eta_{ij} = \delta_{ij}$ or $\eta_{ij} = 1 - \delta_{ij}$, $U_{IJ}(r_{ij})$ and $V_{IJ}(r_{ij})$ are two pair functions, and $F_{IJ}(X_{ij})$ is a function of a local variable X_{ij} that will be discussed below. It can be seen that when $\eta_{ij} = \delta_{ij}$, the summation in equation (7) excludes the self-interaction term $i = j$ and is therefore over all pairs of different atoms. When $\eta_{ij} = 1 - \delta_{ij}$, the second term becomes $E = \frac{1}{2}\sum_{i=1}^{N} F_{II}(X_{ii})\cdot V_{II}(r_{ii})$, which can be used to incorporate the embedding energy of the embedded-atom method as will be clear later in this section. The variable X_{ij} essentially accounts for the environment surrounding the ij bond, and is defined as

$$X_{ij} = \sum_{\substack{k=i_1 \\ k\neq i,j}}^{i_N} W_{IK}(r_{ik})\cdot G_{JIK}(\theta_{jik})\cdot P_{IK}(\Delta r_{jik}) \tag{8}$$

where $P_{IJ}(\Delta r_{jik})$ is a function of weighted difference between atomic spacing r_{ij} and r_{ik}, which is written as $\Delta r_{jik} = r_{ij} - \xi_{IJ}\cdot r_{ik}$ with the weighting factor ξ_{IJ} being either 0 or 1 to include or exclude

r_{ik}, $W_{IK}(r_{ik})$ is another pair function, and $G_{JIK}(\theta_{jik})$ is a three-body function of bond angle θ_{jik}. It can be seen that this polymorphic interatomic potential model is fully defined when the indicators η_{ij} and ξ_{IJ}, and the six functions $U_{IJ}(r)$, $V_{IJ}(r)$, $P_{IJ}(\Delta r)$, $W_{IJ}(r)$, $F_{IJ}(X)$, and $G_{JIK}(\theta)$ (for all the species I, J, K = 1, 2, …) are given. Note that these six functions can all be supplied as one-dimensional tables and can therefore be implemented in MD codes using cubic spline interpolation and/or extrapolation. As a result, users can easily perform simulations using different potentials by tabulating these functions (in a MD read-in table file) accordingly. For instance, the polymorphic potential reduces to our MSW potential if we tabulate the functions according to:

$$\begin{cases} \eta_{ij} = \delta_{ij}, \xi_{IJ} = 0 \\ U_{IJ}(r) = \phi_{R,IJ}(r) - \phi_{A,IJ}(r) \\ V_{IJ}(r) = u_{IJ}(r) \\ F_{IJ}(X) = -X \\ P_{IJ}(\Delta r) = 1 \\ W_{IJ}(r) = u_{IJ}(r) \\ G_{JIK}(\theta) = g_{JIK}(\theta) \end{cases} \tag{9}$$

where $\phi_{R,IJ}(r)$, $\phi_{A,IJ}(r)$, $u_{IJ}(r)$, and $g_{JIK}(\cos\theta)$ are defined by Eqs. (2), (3), (5) and (6). The polymorphic potential reduces to a conventional SW [33] potential if we tabulate the functions according to:

$$\begin{cases} \eta_{ij} = \delta_{ij}, \xi_{IJ} = 0 \\ U_{IJ}(r) = A_{IJ} \cdot \varepsilon_{IJ} \cdot \left(\dfrac{\sigma_{IJ}}{r}\right)^{q} \cdot \left[B_{IJ}\left(\dfrac{\sigma_{IJ}}{r}\right)^{p-q} - 1\right] \cdot \exp\left(\dfrac{\sigma_{IJ}}{r - a_{IJ} \cdot \sigma_{IJ}}\right) \\ V_{IJ}(r) = \sqrt{\lambda_{IJ} \cdot \varepsilon_{IJ}} \cdot \exp\left(\dfrac{\gamma_{IJ} \cdot \sigma_{IJ}}{r - a_{IJ} \cdot \sigma_{IJ}}\right) \\ F_{IJ}(X) = -X \\ P_{IJ}(\Delta r) = 1 \\ W_{IJ}(r) = \sqrt{\lambda_{IJ} \cdot \varepsilon_{IJ}} \cdot \exp\left(\dfrac{\gamma_{IJ} \cdot \sigma_{IJ}}{r - a_{IJ} \cdot \sigma_{IJ}}\right) \\ G_{JIK}(\theta) = \left(\cos\theta + \dfrac{1}{3}\right)^2 \end{cases} \tag{10}$$

where A_{IJ}, B_{IJ}, ε_{IJ}, σ_{IJ}, λ_{IJ}, γ_{IJ}, a_{IJ}, p, and q are the normal parameters for the SW potential as described above. The polymorphic model represents Tersoff types of potential [39,40] if we set

$$\begin{cases} \eta_{ij}=\delta_{ij},\xi_{IJ}=1 \\ U_{IJ}(r)=\dfrac{D_{e,IJ}}{S_{IJ}-1}\exp\left[-\beta_{IJ}\sqrt{2S_{IJ}}\left(r-r_{e,IJ}\right)\right]\cdot f_{c,IJ}(r) \\ V_{IJ}(r)=\dfrac{S_{IJ}\cdot D_{e,IJ}}{S_{IJ}-1}\exp\left[-\beta_{IJ}\sqrt{\dfrac{2}{S_{IJ}}}\left(r-r_{e,IJ}\right)\right]\cdot f_{c,IJ}(r) \\ F_{IJ}(X)=\left(1+X\right)^{-\frac{1}{2}} \\ P_{IK}(\Delta r)=\exp\left[2\mu_{IK}\cdot\Delta r\right] \\ W_{IK}(r)=f_{c,IK}(r) \\ G_{JIK}(\theta)=\gamma_{IK}\left[1+\dfrac{c_{IK}^2}{d_{IK}^2}-\dfrac{c_{IK}^2}{d_{IK}^2+\left(h_{IK}+\cos\theta\right)^2}\right] \end{cases} \tag{11}$$

where $f_{c,IJ}(r_{ij})$ is a cutoff function defined as

$$f_{c,IJ}(r)=\begin{cases}1, & r\le r_{s,IJ}\\ \dfrac{1}{2}+\dfrac{1}{2}\cos\left[\dfrac{\pi(r-r_{s,IJ})}{r_{c,IJ}-r_{s,IJ}}\right], & r_{s,IJ}<r<r_{c,IJ}\\ 0, & r\ge r_{c,IJ}\end{cases} \tag{12}$$

and $D_{e,IJ}$, S_{IJ}, $r_{e,IJ}$, β_{IJ}, μ_{IJ}, γ_{IJ}, c_{IJ}, d_{IJ}, h_{IJ}, $r_{s,IJ}$ and $r_{c,IJ}$ are all pairwise parameters. The polymorphic potential can also represent the Rockett-Tersoff potential [38] if we set

$$\begin{cases} \eta_{ij}=\delta_{ij},\xi_{IJ}=1 \\ U_{IJ}(r)=\begin{cases}A_{IJ}\cdot\exp\left(-\lambda_{1,IJ}\cdot r\right)\cdot f_{c,IJ}(r), & r\le r_{s,1,IJ}\\ A_{IJ}\cdot\exp\left(-\lambda_{1,IJ}\cdot r\right)\cdot f_{c,IJ}(r)\cdot f_{c,1,IJ}(r), & r_{s,1,IJ}<r<r_{c,1,IJ}\\ 0, & r\ge r_{c,1,IJ}\end{cases} \\ V_{IJ}(r)=\begin{cases}B_{IJ}\cdot\exp\left(-\lambda_{2,IJ}\cdot r\right)\cdot f_{c,IJ}(r), & r\le r_{s,1,IJ}\\ B_{IJ}\cdot\exp\left(-\lambda_{2,IJ}\cdot r\right)\cdot f_{c,IJ}(r)+A_{IJ}\cdot\exp\left(-\lambda_{1,IJ}\cdot r\right)\cdot f_{c,IJ}(r)\cdot\left[1-f_{c,1,IJ}(r)\right] & r_{s,1,IJ}<r<r_{c,1,IJ}\\ B_{IJ}\cdot\exp\left(-\lambda_{2,IJ}\cdot r\right)\cdot f_{c,IJ}(r)+A_{IJ}\cdot\exp\left(-\lambda_{1,IJ}\cdot r\right)\cdot f_{c,IJ}(r), & r\ge r_{c,1,IJ}\end{cases} \\ F_{IJ}(X)=\left[1+\left(\beta_{IJ}\cdot X\right)^{n_{IJ}}\right]^{\frac{1}{2n_{IJ}}} \\ P_{IK}(\Delta r)=\exp\left[\lambda_{3,IK}\cdot\Delta r^3\right] \\ W_{IK}(r)=f_{c,IK}(r) \\ G_{JIK}(\theta)=1+\dfrac{c_{IK}^2}{d_{IK}^2}-\dfrac{c_{IK}^2}{d_{IK}^2+\left(h_{IK}+\cos\theta\right)^2} \end{cases} \tag{13}$$

where $f_{c,1,IJ}(r)$ is a cutoff function similar to equation (12) but operates at a different cutoff range:

$$f_{c,1,IJ}(r)=\begin{cases}1, & r\le r_{s,1,IJ}\\ \dfrac{1}{2}+\dfrac{1}{2}\cos\left[\dfrac{\pi(r-r_{s,1,IJ})}{r_{c,1,IJ}-r_{s,1,IJ}}\right], & r_{s,1,IJ}<r<r_{c,1,IJ}\\ 0, & r\ge r_{c,1,IJ}\end{cases} \tag{14}$$

and A_{IJ}, B_{IJ}, $\lambda_{1,IJ}$, $\lambda_{2,IJ}$, $\lambda_{3,IJ}$, β_{IJ}, n_{IJ}, c_{IJ}, d_{IJ}, h_{IJ}, $r_{s,1,IJ}$, and $r_{c,1,IJ}$ are all pairwise parameters. To use the polymorphic model for the embedded-atom method potential [42], we can simply set:

$$\begin{cases} \eta_{ij} = 1 - \delta_{ij}, \xi_{IJ} = 0 \\ U_{IJ}(r) = \phi_{IJ}(r) \\ V_{IJ}(r) = 1 \\ F_{II}(X) = -2F_I(X) \\ P_{IK}(\Delta r) = 1 \\ W_{IK}(r) = f_K(r) \\ G_{JIK}(\theta) = 1 \end{cases} \quad (15)$$

where $\phi_{IJ}(r)$ is a pair function, $f_J(r)$ is an atomic electron density function, $F_I(X)$ is the embedding energy function, and X is used to represent electron density ($X = \rho$). We have implemented and released this polymorphic potential model in the public parallel MD code, LAMMPS [22], and have received positive feedbacks from the research committee.

V. ***Parameterization***

To enable structure evolution of ionic materials to be studied within the short time scales of MD simulations, we attempt to accelerate ionic migration by external electric fields. Such electric fields are approximated by applying opposite external forces to cations and anions. To ensure that the interatomic potential is robust enough to maintain the equilibrium crystal structure of TlBr when Tl+ and Br^- ions are subject to large external forces, we require that the potential not only best captures the key experimental properties of the observed Tl, Br, and TlBr phases (e.g., Tl-hcp, TlBr-CsCl, etc.), but also predicts the crystalline growth of the ground state structures during MD simulations of growth (e.g., vapor deposition). Note that a potential is said to be incapable of crystalline growth simulations only when it predicts amorphous growth at all combinations of temperatures and growth rates possible with the MD simulations. At low temperatures and high growth rates where earlier adatoms are buried by later adatoms before the surface reaches a low energy configuration, amorphous growth is the correct prediction. The growth simulation tests are important because they sample a variety of configurations (at the growth surface) not considered a prior. If any of the random nuclei formed on the growth surface has a lower energy than the growth crystal, the simulations is likely to always give an amorphous growth regardless of temperature and growth rate. Hence, crystalline growth provides strong validation that the growth crystal has the lowest energy compared to any other configurations. When the equilibrium TlBr crystal has the lowest energy, large external forces can be applied to Tl+ and Br- ions without causing phase transformation. Hence, the growth simulation capability is essential for our applications.

We proceed by parameterizing first the Tl and Br potentials, and then the TlBr potential at the known Tl and Br parameters. The observed room-temperature equilibrium phases are hcp for Tl [45] , diatomic (Br_2) liquid for Br, and CsCl for TlBr [44]. Note that solid Br has an orthorhombic crystal structure; however, Br_2 liquid is the stable room-temperature phase. Like many other potentials, our MSW model is not intended to capture the Br_2 molecules (it is possible to capture the Br_2 molecules, but this does not necessarily result in a better potential). On the other hand, our density function theory (DFT) calculations, employing the optB86b-vdW functional (see the Appendix of this Chapter), indicated that the sc Br phase has a lower cohesive energy than dc, bcc, fcc, and hcp phases. Hence, we target sc as the lowest energy lattice phase for Br (at 0 K)

while at the same time ensure that the stable Br phase at room temperature is liquid. Note that if a correct negative heat of formation of the TlBr compound is captured, elemental phases do not form in MD simulations under stoichiometric conditions. Because they do not form, particular elemental structures are not important for studying stoichiometric compounds.

Lattice constants, cohesive energies, and elastic constants for the model lowest energy lattices (Tl-hcp, Br-sc, and TlBr-CsCl) are fitted under the constraints that the energies of all the other phases (e.g., dc, bcc, fcc, NaCl, wz, etc.) are higher than the targeted lowest energy phases. For the experimentally observed structures such as Tl-hcp and TlBr-CsCl, the experimental lattice constants [44], cohesive energies [46], and elastic constants [47,48] are directly used as the target values for the fitting. For the phases that are not observed (e.g., Br-sc), the available experimental properties of other phases and DFT results are used to guide the selection of the target values. In particular, DFT results may be quite different from the experimental values. For example, the hcp Tl cohesive energy obtained from experiments and DFT calculations is -1.85 and -2.40 eV/atom respectively. As a result, we scale the DFT results so that for the observed structures, the scaled DFT results match the experiments.

The software package Mathematica [49] is used to perform the parameterization. To promote global optimization, four different numerical optimization routines, namely a conjugate gradient method [50], the downhill simplex method of Nelder and Mead [51], a genetic algorithm [52], and a biased random walk (simulated annealing) [53], are all used to determine the parameters that minimize the weighted mean-square deviation between the target and predicted properties. The goal to capture the crystalline growth is more challenging, requiring a highly iterative parameterization process. After each fitting iteration, the four sets of parameters from the four optimization routines are tested for vapor deposition simulations. If the potential does not pass these tests, the entire process is repeated with an appropriate adjustment of parameters bounds, target structures and target properties. The iterations continue until one of the four optimization routines results in a satisfactory set of potential parameters. The MSW potential thus determined is listed in Tables 1 and 2 for two-body, and three-body parameters respectively.

Table 1. Two-body parameters of MSW potential (length in Å and energy in eV).

IJ	$r_{0,IJ}$	$r_{s,IJ}$	$r_{c,IJ}$	$E_{b,IJ}$	$\alpha_{,IJ}$	$\beta_{,IJ}$	$\gamma_{,IJ}$
TlTl	3.02409	3.97219	4.26900	-0.514663	5.60012	3.39397	1.94224
BrBr	2.83451	3.60000	4.05800	-0.336014	7.00000	4.37500	3.00000
TlBr	2.98521	3.90480	4.73600	-0.747107	6.20000	2.00000	2.20000

Table 2. Three-body parameters of MSW potential (length in Å and energy in eV).

IJK	TlTlTl	BrBrBr	TlTlBr (=BrTlTl)	TlBrBr (=BrBrTl)	TlBrTl	BrTlBr
λ_{JIK}	0.05000	0.13144	0.11804	0.05733	2.38107	2.38107
$\cos\theta_{0,JIK}$	0.07257	-0.50000	-0.53735	-0.54059	-0.29333	-0.29333
$\cos\theta_{1,JIK}$	-1.00000	-1.00000	-1.00000	-1.00000	-1.00000	-1.00000
$\cos\theta_{2,JIK}$	0.60000	0.60000	0.53947	0.56717	0.29333	0.29333
$\xi_{0,JIK}$	3.50000	0.62340	1.44291	2.79355	0.25182	0.25182
$\xi_{1,JIK}$	0.18625	2.60000	0.70848	1.42550	0.24026	0.24026
$\xi_{2,JIK}$	0.00000	0.00000	1.72178	2.04092	0.46849	0.46849

$\kappa_{1,JIK}$	0.20957	0.96000	1.00000	0.75390	1.00000	1.00000
$\kappa_{2,JIK}$	0.00000	0.00000	0.00000	0.27602	0.94796	0.94796

VI. Evaluation of the Potential

1. Lattice Constants and Cohesive Energies

Our objective is to study the equilibrium TlBr crystal under the stoichiometric condition where no other phases occur, so that the critical properties are for the TlBr-CsCl crystal. With this in mind, calculations based on the polymorphic potential model are performed to evaluate our TlBr potential. First, lattice constants and cohesive energies of various Tl, Br, and TlBr lattices are calculated using energy minimization simulations. The results are summarized in Table 3 along with the available experimental data and our DFT values.

Table 3. Lattice constants a (for dimer, a refers to the dimer bond length) and c (Å), and cohesive energy E_c (eV/atom), obtained from the MSW potential, DFT calculations, and experiments for selected material structures.

material	structure	MSW			DFT (HSE06)			Exp.		
		a	c	E_c	a	c	E_c	a [44]	c [44]	E_c [45]
Tl	dc	7.180	-----	-0.999	7.012	----	-1.526	-----	-----	-----
	sc	3.012	-----	-1.800	3.214	----	-1.827	-----	-----	-----
	bcc	3.854	-----	-1.805	3.971	----	-1.828	-----	-----	-----
	fcc	4.825	-----	-1.848	4.940	----	-1.927	-----	-----	-----
	hcp	3.408	5.582	-1.850	3.558	5.674	-1.874	3.450	5.520	-1.850
Br	di (gas)	-----	-----	-----	2.272	----	-1.132	-----	-----	-0.986
	dc	6.591	-----	-0.731	7.078	----	-0.405	-----	-----	-----
	fcc	4.878	-----	-0.748	4.803	----	-0.281	-----	-----	-----
	bcc	3.847	-----	-0.780	3.822	----	-0.361	-----	-----	-----
	hcp	3.328	5.743	-0.787	2.919	----	-0.840	-----	-----	-----
	sc	3.004	-----	-0.827	3.174	----	-0.459	-----	-----	-1.134*
TlBr	wz	4.877	7.964	-1.657	4.994	8.371	-2.473	-----	-----	-----
	zb	6.897	-----	-1.657	7.494	----	-2.450	-----	-----	-----
	NaCl	6.197	-----	-2.239	6.762	----	-2.529	-----	-----	-----
	CsCl	3.985	-----	-2.389	4.032	----	-2.487	3.985	-----	-2.389

*: Br-sc is the lowest energy lattice in models. No experimental data is available for the metastable Br-sc phase. Instead, we list the experimental cohesive energy of the lowest energy phase (Br_2-liquid) as a reference.

Table 3 indicates that of the lattice structures explored, our MSW potential captures the Tl-hcp and TlBr-CsCl lattice crystals as the lowest energy phases, in agreement with experiments that Tl-hcp and TlBr-CsCl phases are observed at room temperature. Table 3 also indicates that our MSW potential captures the lowest energy for the Br-sc crystal, which is really the target of the MSW model. We cannot include the Br_2 liquid observed in experiments in Table 3. Instead, we will show below through growth simulations that our potential gives Br liquid as the most stable

phase at room temperature. Here we can see that in addition to capturing appropriate lowest energy phases, our MSW model also reproduces the experimental cohesive energies of Tl-hcp and TlBr-CsCl. Our energy of -0.827 eV/atom for Br-sc is not unreasonable compared with the experimental cohesive energy of -1.134 eV/atom for a more stable Br_2-liquid, especially considering that this difference between MSW and experiments is not much more significant than that between DFT and experiments, not to mention that the elemental Br phase does not occur for our intended problem. Note that MSW model also accurately captures the experimental lattice constant of TlBr-CsCl. The lattice constants of Br-sc and Tl-hcp as determined by our MSW is not far off from the experimental or DFT values either (in case of Tl-hcp, for example, while the lattice constant *a* is slightly under-estimated, the lattice constant *c* is slightly over-estimated resulting in a good description of atomic volume).

Capturing non-tetrahedral crystals (such as hcp, sc, CsCl) as the lowest energy phases proves that the MSW potential is more flexible than the conventional SW potentials. SW potentials are not designed for capturing property trends of a variety of metastable structures. The purpose of listing some selected metastable phases in Table 3 is to show that the equilibrium phases have lower energies than these metastable phases. Interestingly, however, our MSW potential reproduces the DFT order of Tl structures with increasing (more negative) cohesive energies as in dc $\rightarrow$ sc $\rightarrow$ bcc $\rightarrow$ fcc. Furthermore, our MSW model correctly captures the lowest energy for Tl-hcp whereas the DFT does not. This observation suggests that MSW potential can possess good transferability to a variety of other phases. Usually such transferability is only possible with more sophisticated potentials. Since our MSW is designed for studying the TlBr bulk, the transferability to many metastable phases is not relevant and so we do not exploit this further for the Br and TlBr phases which would necessarily sacrifice the properties of the equilibrium phases.

Finally, we point out that Table 3 only explores limited number of phases and therefore does not prove that the predicted lowest energy phases indeed have the lowest energies as compared to any other configurations. As will be discussed below, we will prove this rigorously through vapor deposition simulations.

2. Elastic Constants and Melting Temperature

Elastic constants and melting temperature of the experimentally observed Tl-hcp and TlBr-CsCl phases are calculated, and the results are summarized in Table 4 along with the experimental values. Here the melting temperature calculations follow the same method described previously [34,37,54,55,56]. It can be seen that our MSW model reproduces the experimental elastic constants for TlBr-CsCl. The model elastic constants for Tl-hcp are generally lower than the experimental values. Note that we could have fit exactly the experimental elastic constants for Tl-hcp. However, this would result in a melting temperature that is significantly above the experimental value. On the other hand, the conventional SW potentials tend to significantly overestimate elastic constants for closely packed elements and hence the ability to prescribe low elastic constants is significant for the MSW model.

Table 4. Elastic constants C_{11}, C_{12}, C_{13}, C_{33}, C_{44}, bulk modulus B (eV/Å^3), and melting temperature T_m (K) of the observed Tl and TlBr crystalline phases, obtained from the MSW potential and experiments.

structure	method	C_{11}	C_{12}	C_{13}	C_{33}	C_{44}	B	T_m
Tl (hcp)	MSW	0.240	0.140	0.137	0.242	0.053	0.133	691
	Exp. [46,57]	0.277	0.235	0.187	0.376	0.055	0.239	577
TlBr (CsCl)	MSW	0.275	0.104	0.104	0.275	0.067	0.161	1442
	Exp. [47,58]	0.275	0.104	0.104	0.275	0.067	0.161	753

We get the melting temperature of Tl-hcp reasonably close to the experimental value. Despite a prolonged effort, our current parameterization of the MSW potential still significantly overestimates the melting temperature of TlBr-CsCl. We can better capture the melting temperature by reducing the elastic constants. Considering that our objective is to study the behavior of the TlBr-CsCl crystal at ambient temperature, we chose to capture exactly the elastic constants at the cost of overestimating the melting temperature. We feel that this problem cannot be resolved by parameterization alone, and further modifications of the MSW format are needed in future efforts in order to capture both elastic constants and melting temperature.

3. Point Defects

Native point defects in TlBr-CsCl, including Tl vacancy V_{Tl}, Br vacancy V_{Br}, Tl at Br antisite Tl_{Br}, Br at Tl antisite Br_{Tl}, Tl interstitial between Tl sites $Tl_{i,1}$, Tl interstitial between Br sites $Tl_{i,2}$, Br interstitial between Tl sites $Br_{i,1}$, and Br interstitial between Br sites $Br_{i,2}$, are all studied. In particular, intrinsic defect energies $E_D^{'}$ are calculated as [59,60]

$$E_D^{'} = E - (N_{Tl} + N_{Br}) \cdot E_{TlBr} - 0.5 \cdot (N_{Tl} - N_{Br}) \cdot (E_{Tl} - E_{Br}) \quad (16)$$

where E, N_{Tl}, and N_{Br} are total energy, number of Tl atoms, and number of Br atoms of the system containing the defect, and E_{TlBr}, E_{Tl}, and E_{Br} are cohesive energies (per atom unit) for the lowest energy phases of TlBr, Tl, and Br respectively. The results obtained from MSW and DFT calculations are summarized in Table 5. It can be seen that MSW potential predicts a lower energy for Tl vacancy than for Br vacancy, a lower energy for Br at Tl antisite than for Tl at Br antisite, and a lower energy for $Br_{i,2}$ interstitial than for both Tl interstitials. All these are in good agreement with the DFT calculations. Our MSW potential indicates that the $Br_{i,1}$ interstitial has a lower energy than both Tl interstitials, which differs from the DFT result that the $Br_{i,1}$ interstitial energy is only lower than the $Tl_{i,2}$ interstitial energy. Again here we only compare the trends, and do not make conclusions on the absolute values due to the lack of experimental data.

Table 5. Intrinsic defect energy $E_D^{'}$ (eV) obtained from different models for TlBr-CsCl. The DFT results were determined using the HSE06 functional based on the optB86b-vdW optimized geometries (see Appendix for details).

method	V_{Tl}	V_{Br}	Tl_{Br}	Br_{Tl}	$Tl_{i,1}$	$Tl_{i,2}$	$Br_{i,1}$	$Br_{i,2}$
MSW	1.04	1.29	2.75	1.05	2.93	3.03	2.00	2.00
DFT	1.24	1.81	3.59	3.02	1.85	2.82	2.69	1.74

VII. ***Vapor Deposition Verification***

As mentioned above, only when a potential captures the crystalline growth during MD vapor deposition simulations will it capture the lowest energy phase and be robust enough to allow

applications of high external electric fields. Here we perform vapor deposition simulations to validate that our TlBr MSW potential captures the crystalline growth of the lowest energy Tl-hcp and TlBr-CsCl crystals. In addition, we will demonstrate that our potential gives the crystalline growth of Br-sc at a low temperature (this is the lowest energy "model" phase as opposed to the orthorhombic experimental lowest energy phase) but gives a liquid Br structure as the stable phase at room temperature.

1. Tl-hcp Growth

For Tl-hcp growth, an initial substrate of an hcp crystal containing 1008 Tl atoms with 28 $(2\bar{1}\bar{1}0)$ layers in the x direction, 9 (0002) layers in the y direction, and 8 $(0\bar{1}10)$ layers in the z direction is used. Here layers refer to crystallographic planes so that one (0001) layer is equivalent n (000n) layers etc. The substrate temperature is set at T = 300 K by assigning velocities to atoms according to the Boltzmann distribution. During simulations, the bottom (-y) 2 (0002) layers are held fixed to prevent crystal shift upon adatom impact on the top surface. The next 3 (0002) layers are isothermally controlled at the substrate temperature. This leaves the top 4 layers free where the motion of atoms is solely determined by Newton's law. Injection of Tl adatoms from random locations far above the surface simulates the growth. All adatoms have an initial far-field incident kinetic energy E_i = 0.05 eV and an incident angle $\theta = 0^o$ (i.e., the moving direction is perpendicular to the surface). The adatom injection frequency is chosen to give a deposition rate of R = 2.5 nm/ns. To approximately maintain a constant thickness of the free surface region, the isothermal region expands upward during simulations. Since surface roughness might develop, the isothermal region expands at about 80% of the surface growth rate to ensure that the upper boundary of the isothermal region never exceeds the surface valley locations. Fig. 1 shows the resulting configuration obtained after 0.66 ns deposition, where the original substrate is shaded in purple. It can be seen that the MSW potential correctly captures the crystalline growth of the Tl-hcp phase. This strongly validates that Tl-hcp has the lowest energy at room temperature as compared to any other configurations.

2. Br-sc Growth

MD simulations are also performed to grow Br on an Br-sc substrate. A sc crystal containing 1008 Br atoms with 14 (100) layers in the x direction, 9 (010) layers in the y direction, and 8 (001) layers in the z direction is used as the initial substrate. During simulations, the bottom 2 (020) layers are held fixed. The next 4 (020) layers are controlled at the desired growth temperature. Using the same approach as described above, the growth simulation is performed at two substrate temperatures T = 150 K and T = 300 K, an incident energy E_i = 0.05 eV, an incident angle $\theta = 0^o$, and a deposition rate R = 2.5 nm/ns. The resulting configurations obtained after 1.20 ns deposition are shown in Figs. 2(a) and 2(b) respectively for the 150 K and 300 K temperatures. It can be seen from Fig. 2(a) that the sc- crystalline growth is achieved with our potential, strongly validating that the Br-sc crystal has the lowest (free) energy at 150 K as compared to any other configurations. Fig. 2(b), on the other hand, shows that amorphous growth is achieved at 300 K. This strongly validates that Br exhibits a liquid phase at room temperature.

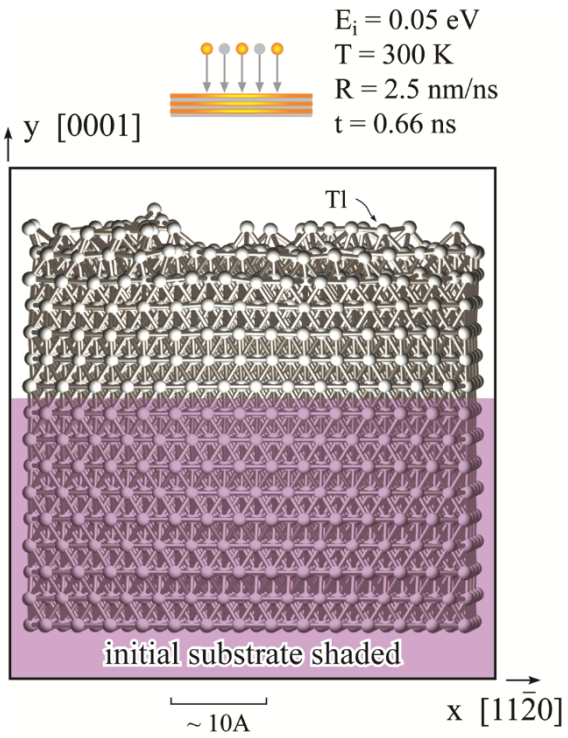

Figure 1. Vapor deposited hcp Tl film obtained from MD simulations.

3. TlBr-CsCl Growth

For TlBr-CsCl growth, an initial TlBr substrate of a CsCl type of crystal containing 300 Tl atoms and 300 Br atoms with 20 (200) layers in the x direction, 10 (020) layers in the y direction, and 12 (002) layers in the z direction is used. Initially, Br terminates the top y surface. During the simulations, the bottom 3 (020) layers are fixed. The next 4 (020) layers are used to control the growth temperature. Following the same approach as described above, the growth simulations are performed at a substrate temperature T = 700 K, an incident energy E_i = 0.05 eV, an incident angle $\theta = 0^o$, a deposition rate R = 2.75 nm/ns, and a stoichiometric vapor flux ratio Tl:Br = 1:1. Fig. 3 shows the system configuration obtained at 0.78 ns deposition time. It is seen again that our MSW potential correctly captures the crystalline growth of the equilibrium (CsCl) phase of TlBr. In particular, the randomly injected Tl and Br atoms are reconstructed correctly to their corresponding sublattices. Because the potential captures the crystallization from a rather stochastic vapor phase, it enables robust simulations of structural evolution of TlBr-CsCl under conditions where the presence of both dislocations and external electric fields may induce configuration disorders if the potential has any deficiencies in capturing the lowest energy phase.

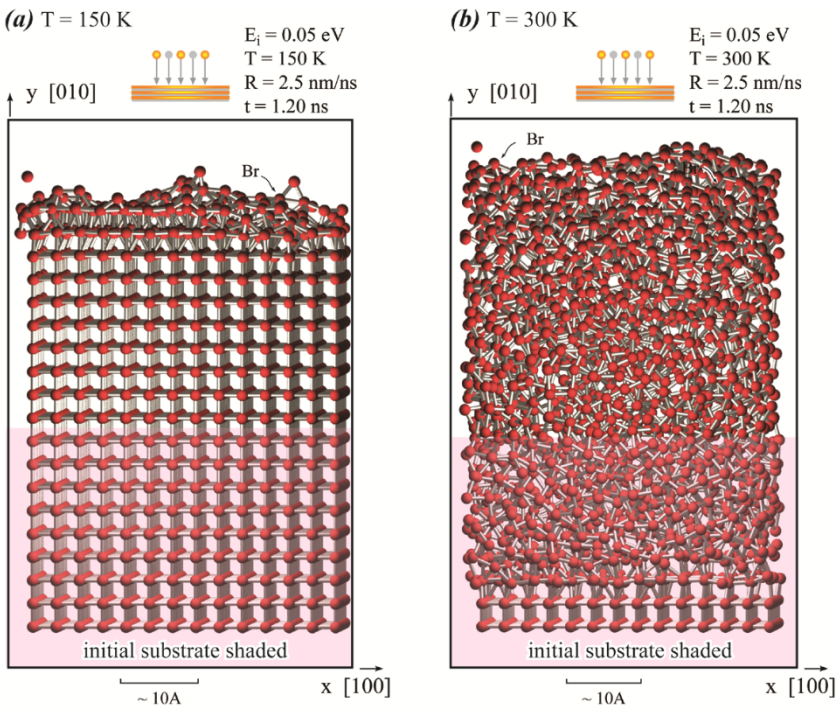

Figure 2. MD simulations of Br growth on a Br-sc substrate at a temperature of (a) 150 K and (b) 300 K. Our potential prescribes a liquid Br as the most stable phase at room temperature.

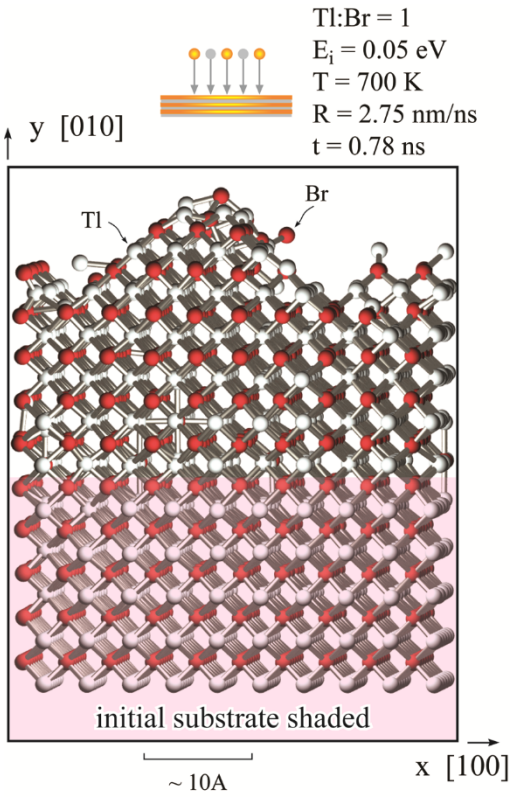

Figure 3. Vapor deposited CsCl phase of a TlBr film obtained from MD simulations.

VIII. ***Electrical Field Verification***

Our objective is to allow direct MD simulations of structural evolution of TlBr-CsCl crystal under an external electric field. The external electric field can be simulated by applying opposite biased forces to Tl and Br atoms. Note that in our model, we do not directly address charges. This is a reasonable approximation because charges only give two forces: the Coulomb forces between atoms, and biased forces under external fields. The Coulomb forces between atoms are digested into the interatomic potential in our model. This allows us to use biased forces to independently simulate the external electric field.

The simulations may become challenging at large external electric fields because the biased forces may induce phase transformation when the potential does not capture the lowest energy for the equilibrium phase. Here we demonstrate two cases to demonstrate that our potential allows simulations to be performed when atoms are subject to large forces of ±0.4 eV/Å. These forces correspond to a high electric field of 4×10^6 V/mm assuming Tl and Br atoms adopt full charges of ±1 e. Again note that atoms are not strictly point charges and atoms in perfect bulk may not be subject to big forces from the external field. Nonetheless, the model becomes robust if we pass this test.

A TlBr-CsCl crystal containing 16128 Tl atoms and 16128 Br atoms with 84 $(1\bar{1}0)$ layers in the x direction, 24 $(\bar{1}10)$ layers in the y direction, and 32 (002) layers in the z direction is used. To prevent system from shifting, the bottom region of about 10 Å wide is fixed. To remove the boundary effects, periodic boundary conditions are used in all three coordinate directions. An MD simulation is then performed at 1200 K (a homologous temperature 0.832 T_m) with a biased force of ±0.4 eV/Å using the NVT ensemble (i.e., number of atoms, volume, and temperature are all constant).

In the first case, we assume that the system contains a pair of Tl and Br vacancies by removing a Tl and a Br atom far away from the fixed region. Comparison of atomic configurations between a time span of 0.06 ns is shown in Fig. 4. Fig. 4 verifies that our potential allows for stable TlBr-CsCl MD simulations to be performed with a high biased force. Interestingly, we found that Tl and Br vacancies are not very mobile even at the high biased force and temperature. In fact, during the 0.06 ns span, Tl vacancy jumped by one lattice spacing whereas the Br vacancy did not jump.

In the second case, we assume that the system contains a pair of Tl and Br interstitials by inserting a Tl atom and a Br atom at locations far away from the fixed region. Comparison of atomic configurations between a time span of 0.12 ns is shown in Fig. 5. Fig. 5 again verifies that our potential allows stable TlBr-CsCl MD simulations to be performed with a high biased force. Unlike the vacancy case, we found that Tl and Br interstitials are very mobile, and both interstitials moved a significant distance during the 0.12 ns time span.

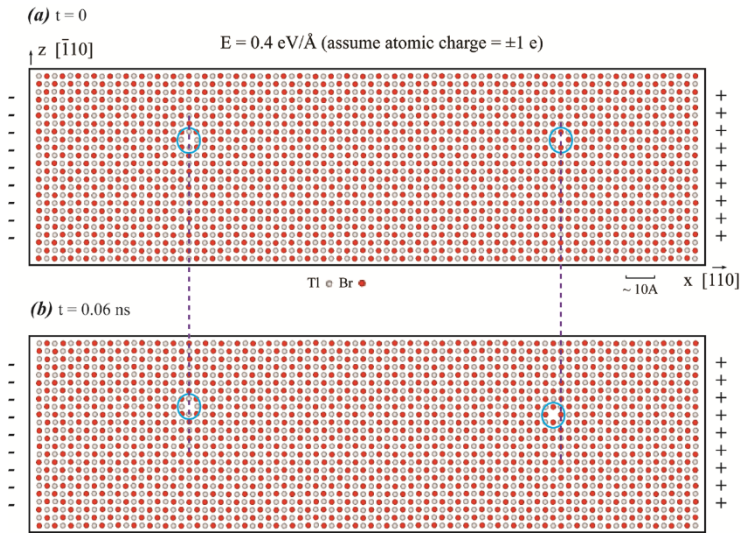

Figure 4. Structure evolution of a TlBr-CsCl crystal containing vacancies at a temperature of 0.832 T_m and a biased force of ±0.4 eV/Å: (a) Starting time of observation; and (b) 0.06 ns later. The TlBr-CsCl crystal remains intact at the large electric field. During the 0.06 ns span, Tl vacancy jumped by one lattice spacing whereas the Br vacancy did not jump.

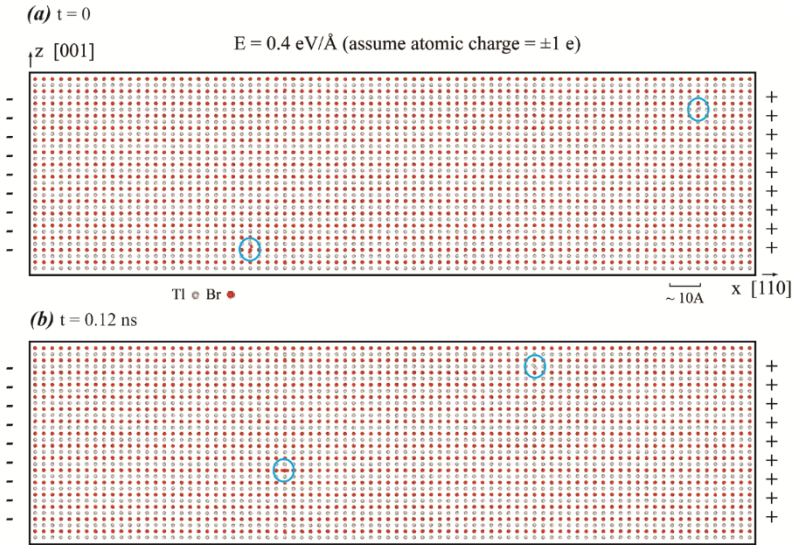

Figure 5. Structure evolution of a TlBr-CsCl crystal at a temperature of 0.832 T_m and a biased force of ±0.4 eV/Å: (a) Starting time of observation; and (b) 0.12 ns later. The TlBr-CsCl crystal remains intact at the large electric field. During the 0.12 ns span, Tl and Br interstitials migrated significant distances.

The cases shown in Figs. 4 and 5 are designed to validate the robustness of our potential, but not to launch a thorough study of structure deterioration under external fields. Such thorough studies will be presented in Chapters 4 and 5.

IX. ***Conclusions***

Herein we have developed a new modified Stillinger-Weber potential. Unlike the conventional SW potential that significantly overestimates the elastic constants of closely packed elements and are limited mainly to tetrahedral structures, our modified potential can capture very low elastic constants for closely packed elements and can be used for many non-tetrahedral crystal structures. We have parameterized the modified SW potential for TlBr. Through rigorous vapor deposition simulation tests, we have demonstrated that our potential captures the experimental properties of the observed Tl and TlBr phases, and predicts the Br liquid to be the most stable phase at room temperature. Moreover, we have demonstrated that our potential is robust enough for challenging simulations of structure evolution of TlBr crystals under very high external electric fields. Test simulations indicate that interstitials migrate much faster than vacancies. We have also developed a polymorphic potential model and implemented it in the public MD code, LAMMPS. This essentially enables future material research to be performed at a higher fidelity level because improved potentials no longer require modification of the MD codes and therefore can immediately be utilized by a broader materials and physics community.

X. ***Appendix***

Density functional theory calculations are performed within the spin-polarization formalism using the optB86b-vdW functional [61], and the hybrid HSE06 [62] functional with and without the inclusion of the empirical dispersion correction developed by Grimme [63] (the one with the dispersion correction is notated as HSE06+D). The calculations are carried out using projector-augmented-wave (PAW) pseudopotentials and a plane-wave energy cutoff of 500 eV. The atom positions and primitive unit cells of the bulk materials are optimized using the three methods (optB86b-vdW, HSE06, and HSE06+D) until all forces are less than 0.01 eV/Å. The Brillouin zone is sampled using a 10×10×10 and a 5×5×5 gamma-centered Monkhorst-Pack grid respectively. The optimized lattice parameters and cohesive energies are reported in Table 6. For the point defect calculations (see Table 7), 5×5×5 supercells are created from the optB86b-vdW optimized TlBr-CsCl primitive unit cell and the systems are relaxed (atoms only) until all forces are less than 0.01 eV/Å. For these calculations, the Monkhorst-Pack grid is reduced to 2×2×2. The point defect energies ($E_D^{'}$) are reported in Table 7. The point defect energies are also determined at the HSE06 level of theory using the optB86b-vdW optimized geometries and a 1×1×1 k-point grid. Since the point defect structures are based on the optB86b-vdW optimized geometries, the cohesive energies of the lowest energy bulk materials, as needed for the determination of $E_D^{'}$ (see Eq. 16), are also determined based on the optB86b-vdW optimized geometries. This is done to avoid the inclusion of lattice deformation energy in the point defect energy. All calculations are performed using VASP 5.3.5 [64,65,66,67].

The calculations herein are carried out using different methodologies for a couple reasons. First, we want to consider methods (optB86b-vdW and HSE06+D) capable of modeling dispersion interactions (van der Waals forces) since bromine molecules (Br_2) are held together by such interactions. Although, calculations are not explicitly performed on such a system, we find that the inclusion of van der Waals forces have significant effects on the cohesive energies of the bulk Br structures (see Table 6). Second, Klimeš et al. [60] showed that the optB86b-vdw functional outperforms several traditional generalized-gradient approximation (GGA) functionals (e.g. PBE) for the prediction of lattice constants, bulk moduli, and atomization energies for a range of solids and we want to identify a GGA based functional capable of accurately predicting

the lattice constants of TlBr-CsCl. This is desirable because performing hybrid DFT optimizations on large supercells, required for studying point-defects, is extremely computationally demanding. However, hybrid functionals are arguably more accurate than traditional GGA functionals accredited to the inclusion of exact Fock exchange. The results obtained using the optB86b-vdW functional are in relative good agreement with those obtained using the HSE06+D method. Moreover, the lattice constants obtained for TlBr-CsCl and Tl-hcp agree very well with experiment (~1%), and even slightly better than those obtained using the HSE06 and HSE06+D methods. Note, the PBE functional is also considered but the predicted lattice constants are in greater disagreement with experiment. Regarding the prediction of the cohesive energies, the HSE06 functional performs the best. This attributes to a decrease in self-interaction error as a result of using a functional that incorporates exact Fock exchange. We have decided to included only the HSE06 values in the main text for internal consistency and simplicity; however, we have included the results obtained using the different methods here for completeness and for interested readers.

Table 6. Lattice constants a (for dimer, a refers to the dimer bond length) and c (Å), and cohesive energy E_c (eV/atom) determined using optB88b-vdw, HSE06, and HSE06+D functionals.

material	structure	optB86b-vdw			HSE06			HSE06+D		
		a	c	E_c	a	c	E_c	a	c	E_c
Tl	dc	6.965	----	-1.922	7.012	----	-1.526	6.681	----	-1.899
	sc	3.185	----	-2.238	3.214	----	-1.827	3.082	----	-2.371
	bcc	3.868	----	-2.368	3.971	----	-1.828	3.973	----	-2.294
	fcc	4.873	----	-2.340	4.940	----	-1.927	4.868	----	-2.349
	hcp	3.500	5.581	-2.399	3.558	5.674	-1.874	3.521	5.614	-2.289
Br	di (gas)	2.309	----	-1.265	2.272	----	-1.132	2.280	----	-1.132
	dc	6.898	----	-0.961	7.078	----	-0.405	7.031	----	-0.489
	fcc	4.644	----	-1.123	4.803	----	-0.281	4.852	----	-0.496
	bcc	3.703	----	-1.160	3.822	----	-0.361	3.820	----	-0.580
	hcp	2.945	7.049	-1.210	2.919	----	-0.840	2.902	----	-0.947
	sc	3.006	----	-1.218	3.174	----	-0.459	3.150	----	-0.612
TlBr	wz	4.682	8.724	-2.767	4.994	8.371	-2.473	4.897	8.209	-2.686
	zb	7.371	----	-2.662	7.494	----	-2.450	7.371	----	-2.598
	NaCl	6.622	----	-2.866	6.762	----	-2.529	6.616	----	-2.794
	CsCl	3.959	----	-2.880	4.032	----	-2.487	4.066	----	-2.822

Table 7. Intrinsic defect energies $E_D^{'}$ (eV) for TlBr-CsCl determined using optB88b-vdw, HSE06, and HSE06+D functionals.

method	V_{Tl}	V_{Br}	Tl_{Br}	Br_{Tl}	$Tl_{i,1}$	$Tl_{i,2}$	$Br_{i,1}$	$Br_{i,2}$
optB86b-vdw	0.66	1.56	3.47	1.72	2.16	2.55	2.32	1.59
HSE06	1.24	1.81	3.59	3.02	1.85	2.82	2.69	1.74
HSE06+D	1.51	2.24	3.79	2.66	1.70	2.66	2.35	1.70

3. AN ANALYTICAL VARIABLE CHARGE POTENTIAL MODEL

I. ***Abstract***

This Chapter has been published [23]. It develops a novel analytical variable charge model that significantly improves the computational efficiency of variable charge calculations during molecular dynamics simulations.

II. ***Introduction***

Atomic charges in solid materials are not constant, but rather change as atoms move [68,69]. To address this variable charge effect, almost all literature approaches [70,71] require solving atomic charges at each molecular dynamics time step using a separate energy minimization simulation. This results in extremely high computational expenses. On the other hand, atomic charges are fully determined once atom positions are given. This means that atomic charges can be analytically expressed as a function of atom positions. The objective of the present Chapter is twofold: (a) develops an analytical variable charge model that can be used to calculate atomic charges from atom positions without energy minimization simulations; and (b) uses this analytical variable charge model to perform MD simulations of dislocations in TlBr crystals under an electrical field to gain understanding of aging mechanisms.

III. ***Theory***

1. Variable Charge Model

Our variable charge model will be coupled with the polymorphic modified Stillinger-Weber potential [23] developed in the previous Chapter. This means that atomic charges are only used to calculate the electrostatic forces by the external electric field, and the electrostatic forces between atoms are assumed to be already included in the modified Stillinger-Weber potential.

Based on the fundamental physics of electronegativity [68,69], atoms can only become positively (or negatively) charged when they approach atoms with higher (or lower) electronegativity. Hence, identical atoms are charge neutral, and magnitude of charges increases when spacing between atoms with different electronegativities decreases. To capture this physics, we first derive an analytical charge expression for an undisturbed (i.e., no thermal vibration and no defects) binary system based on the literature variable charge concepts [70,71], and then generalize the expression for disturbed systems. As will be seen below, this approximate model is good enough to capture accurately the charges obtained from ab initio calculations.

Assume that an undisturbed binary system contains n_c cation (C) atoms and n_a anion (A) atoms where each cation atom has n_{cc} neighboring cation atoms at a distance r_{cc}, and n_{ca} neighboring anion atoms at a distance r_{ca}, and each anion atom has n_{ac} neighboring cation atoms at a distance r_{ac}, and n_{aa} neighboring anion atoms at a distance r_{aa} (note that $r_{ac} = r_{ca}$). If valences of cations and anions are respectively v_c and v_a, we can further assume $n_c/n_a = v_a/v_c = n_{ac}/n_{ca}$. The total electrostatic energy of the system is then expressed as [70,71]:

$$E = n_c\left(\chi_c q_c + \frac{1}{2}J_c q_c^2\right) + n_a\left(\chi_a q_a + \frac{1}{2}J_a q_a^2\right) + \frac{n_c n_{cc}}{2}q_c^2\varphi(r_{cc}) + \frac{n_a n_{aa}}{2}q_a^2\varphi(r_{aa}) + \left(\frac{n_c n_{ca}}{2} + \frac{n_a n_{ac}}{2}\right)q_c q_a \varphi(r_{ca}) \quad (1)$$

where χ and J are electronegativity and hardness of atoms, and $\varphi(r)$ represents a Coulomb radial function. Note that strictly, $\varphi(r) = 14.4/r$ (in atomic unit) but here it is simply assumed to be a radially-decaying function. Substituting in the charge balance condition $n_c q_c + n_a q_a = 0$, we can solve from $dE/dq_c = 0$ (or $dE/dq_a = 0$) that

$$q_c = \frac{\chi_a - \chi_c}{J_c + \frac{n_{ac}}{n_{ca}}J_a + n_{cc}\varphi(r_{cc}) + \frac{n_{ac}}{n_{ca}}n_{aa}\varphi(r_{aa}) - \frac{n_{ac}}{n_{ca}}n_{ca}\varphi(r_{ca}) - n_{ac}\varphi(r_{ca})} \quad (2)$$

Clearly, Eq. (2) captures the physics that the magnitude of charges increases when the number cation-anion neighbors increase and their spacings decrease. To extend Eq. (2) to a more general case of disturbed lattices, we can think that $n_{cc}\varphi(r_{cc}) = \sum_{j=c_1}^{c_N}\xi_{cj}\varphi(r_{cj})$, $n_{aa}\varphi(r_{aa}) = \sum_{j=a_1}^{a_N}\xi_{aj}\varphi(r_{aj})$, $n_{ca}\varphi(r_{ca}) = \sum_{j=c_1}^{c_N}(1-\xi_{cj})\varphi(r_{cj})$, $n_{ac}\varphi(r_{ac}) = \sum_{j=a_1}^{a_N}(1-\xi_{aj})\varphi(r_{aj})$ respectively, where c_1, c_2, …, c_N is a list of cation's neighbors, a_1, a_2, …, a_N is a list of anion's neighbors, $\xi_{ij} = 1$ when i = j and $\xi_{ij} = 0$ when $i \neq j$ (i, j = c, a). Eq. (2) can then be written as

$$q_c = \frac{n_{ca}(\chi_a - \chi_c)}{n_{ca}J_c + n_{ac}J_a + n_{ca}\sum_{j=c_1}^{c_N}\xi_{cj}\varphi(r_{cj}) + n_{ac}\sum_{j=a_1}^{a_N}\xi_{aj}\varphi(r_{aj}) - n_{ac}\sum_{j=c_1}^{c_N}(1-\xi_{cj})\varphi(r_{cj}) - n_{ca}\sum_{j=a_1}^{a_N}(1-\xi_{aj})\varphi(r_{aj})} \quad (3)$$

If we want to calculate q_c based only on the information around this C atom, we can replace the information around an A atom by averaging the values of the A atoms neighboring to the C atom:

$$q_c = \frac{n_{ca}(\chi_a - \chi_c)}{n_{ca}J_c + n_{ac}J_a + n_{ca}\sum_{j=c_1}^{c_N}\xi_{cj}\varphi(r_{cj}) + n_{ac}\frac{\sum_{j=c_1}^{c_N}\xi_{aj}B(r_{cj})\sum_{k=j_1}^{j_N}\xi_{jk}\varphi(r_{jk})}{\sum_{j=c_1}^{c_N}\xi_{aj}B(r_{cj})} - n_{ac}\sum_{j=c_1}^{c_N}(1-\xi_{cj})\varphi(r_{cj}) - n_{ca}\frac{\sum_{j=c_1}^{c_N}\xi_{aj}B(r_{cj})\sum_{k=j_1}^{j_N}(1-\xi_{jk})\varphi(r_{jk})}{\sum_{j=c_1}^{c_N}\xi_{aj}B(r_{cj})}} \quad (4)$$

where $B(r_{ij})$ is a bond formation function, i.e., $B(r_{ij}) = 1$ when r_{ij} is small and $B(r_{ij})$ decays to zero when r_{ij} increases. In Eq. (4), we can express

$$n_{ca} = \sum_{j=c_1}^{c_N}\xi_{aj}B(r_{cj}), \quad n_{ac} = \frac{\sum_{j=c_1}^{c_N}\xi_{aj}B(r_{cj})\sum_{k=j_1}^{j_N}\xi_{ck}B(r_{jk})}{\sum_{j=c_1}^{c_N}\xi_{aj}B(r_{cj})} \quad (5)$$

Replacing Eq. (5) in Eq. (4) resulting in an analytical expression for cation charges. Similar procedures can be used to derive an expression for the anion charges. Consolidating both expressions, the charge on any (cation or anion) atom can be expressed as

$$q_i = \frac{(\chi_{!i} - \chi_i)\left[\sum_{j=i_1}^{i_N} \xi_{!ij} B(r_{ij})\right]^3}{J_i\left[\sum_{j=i_1}^{i_N} \xi_{!ij} B(r_{ij})\right]^3 + J_{!i}\sum_{j=i_1}^{i_N} \xi_{!ij} B(r_{ij})\left[\sum_{j=i_1}^{i_N} \xi_{!ij} B(r_{ij})\sum_{k=j_1}^{j_N} \xi_{ik} B(r_{jk})\right] + \left[\sum_{j=i_1}^{i_N} \xi_{!ij} B(r_{ij})\right]^3 \cdot \sum_{j=i_1}^{i_N} \xi_{ij}\varphi(r_{ij}) + \left[\sum_{j=i_1}^{i_N} \xi_{!ij} B(r_{ij})\sum_{k=j_1}^{j_N} \xi_{ik} B(r_{jk})\right]\cdot\left[\sum_{j=i_1}^{i_N} \xi_{!ij} B(r_{ij})\sum_{k=j_1}^{j_N} \xi_{jk}\varphi(r_{jk})\right] - \sum_{j=i_1}^{i_N} \xi_{!ij} B(r_{ij})\left[\sum_{j=i_1}^{i_N} \xi_{!ij} B(r_{ij})\sum_{k=j_1}^{j_N} \xi_{ik} B(r_{jk})\right]\cdot \sum_{j=i_1}^{i_N}(1-\xi_{ij})\varphi(r_{ij}) - \left[\sum_{j=i_1}^{i_N} \xi_{!ij} B(r_{ij})\right]^2 \cdot \left[\sum_{j=i_1}^{i_N} \xi_{!ij} B(r_{ij})\sum_{k=j_1}^{j_N}(1-\xi_{jk})\varphi(r_{jk})\right] + \varepsilon} \quad (6)$$

In Eq. (6), !i = a if i = c, and !i = c if i = a, and an offset parameter ε is added to provide additional flexibility. Based on the physical requirement of the shape of the functions, B(r) and φ(r) are chosen to be

$$B(r) = \begin{cases} \dfrac{\exp(-\alpha \cdot r^{\beta}) - \exp(-\alpha \cdot r_c^{\beta})}{\exp(-\alpha \cdot r_f^{\beta}) - \exp(-\alpha \cdot r_c^{\beta})}, & r \le r_c \\ 0, & r > r_c \end{cases}, \quad \varphi(r) = \begin{cases} \Phi \cdot \exp(-\mu \cdot r^{\nu}) & r < r_s \\ 14.4\left[\dfrac{erfc(\eta \cdot r)}{r} - \dfrac{erfc(\eta \cdot r_q)}{r}\right], & r_s \le r \le r_q \\ 0, & r > r_q \end{cases} \quad (7)$$

where r_c and r_q are cutoff distances for the bond formation function B(r) and the Coulomb function φ(r) functions respectively, r_f, r_s, η, Φ are additional independent parameters, and α, β, μ, ν are dependent parameters that can be determined once independent parameters are known. In particular, $\beta = \dfrac{\ln\left[\ln(0.9)/\ln(10^{-8})\right]}{\ln(r_f/r_c)}$, $\alpha = -\dfrac{\ln(0.9)}{r_f^{\beta}}$, and μ, ν are solved from the condition that φ(r) is continuous and has continuous derivative at the junction point r = r_s. Based on the parameters determined below, B(r) and φ(r) are graphically shown in Fig. 6(a). Clearly, B(r) and φ(r) satisfy the physical requirements described above.

2. Parameterization of Variable Charge Model

The variable charge model described above is fitted to the quantum mechanical Born effective charges [72]. Just like the charge in our model, the Born effective charge is defined as the force acting on an atom per unit of external electrical field. The fitted parameters are shown in Table 8. The MD and quantum mechanical charges as a function of lattice strain are compared in Fig. 6(b). It can be seen that MD and quantum mechanical results agree very well. Note that interestingly, the Born effective charges are above the nominal charges of ±1 e.

Table 8. Variable charge parameters

χ_{Te} (V)	χ_{Br} (V)	J_{Te} (V/e)	J_{Br} (V/e)	ε	η
80.327930	146.771980	16.000000	16.000000	2897.1593	0.3000000
r_f (Å)	r_c (Å)	r_q (Å)	r_s (Å)	Φ (eV)	
3.498950	8.614900	8.614900	3.500000	3.000000	

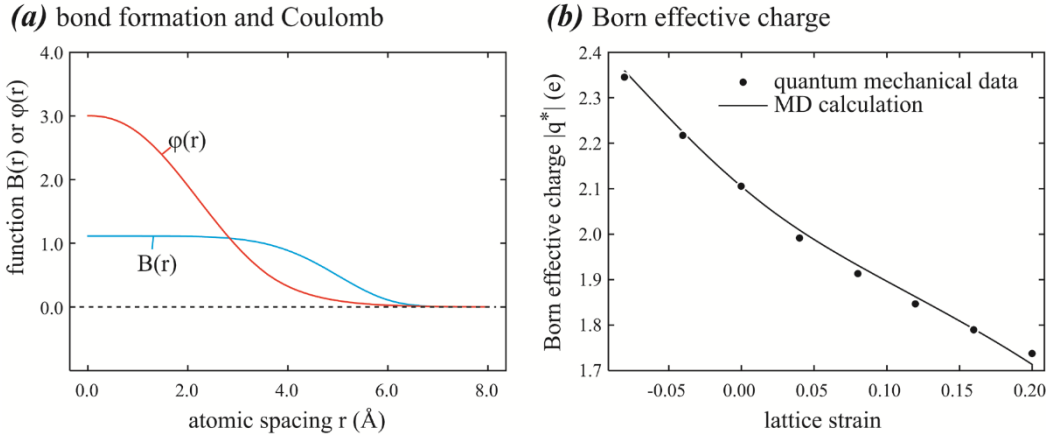

Figure 6. (a) functions B(r) and φ(r) and (b) Born effective charge as a function of lattice strain.

IV. ***Simulations and Results***

As shown in Fig. 7, our simulations apply periodic boundary conditions to a CsCl-type of TlBr crystal containing 60(100) planes in the x direction, 36(010) planes in the y direction, and 56(001) planes in the z direction. A pair of edge dislocations with a perfect Burgers vector of [100] are created by removing 1(100) plane, or equivalently, 2(200) planes, between a distance d of 18(010) planes in the y direction. We point out that due to alternating stacking between Tl and Br atoms in the y direction, the two dislocations are not equivalent. The upper dislocation is Tl-rich at the core (i.e., the leading row of the extra plane is Tl), and is termed an α dislocation. Similarly, the low dislocation is Br-rich and is termed a β dislocation. MD simulations are performed at 900 K using an NVT ensemble (constant number of atoms, volume, and temperature) for a total of 0.6 ns. Note that the interatomic potential defines a melting temperature of 1442 K, which is well above the simulated temperature. An external electrical field of E = 0.06 V/Å is simulated by applying biased forces of $f_i = q_i \cdot E$ to all atoms (i = 1, 2, …). Here the charge q_i is calculated from Eq. (6), and the biased force aligns with +x or –x direction for positive or negative q_i respectively. To prevent the crystal from shifting during long time simulations, atoms in a small region near the origin point (0,0,0) are fixed.

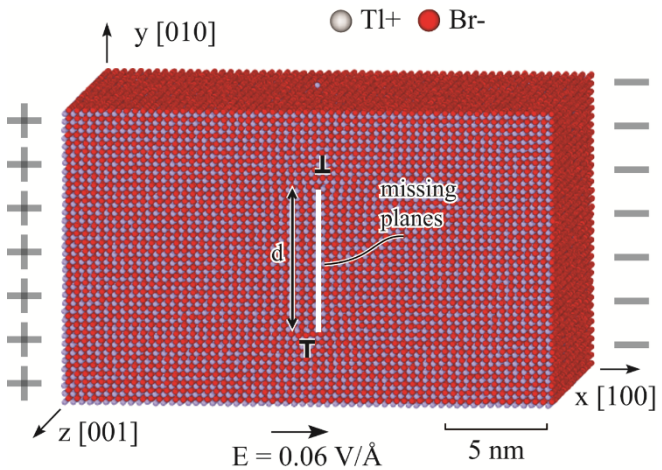

Figure 7. Geometry of MD simulations of dislocations under an electrical field.

MD configurations obtained at different times are analyzed using the dislocation extraction algorithm developed and incorporated in the visualization software OVITO by Stukowski [73]. Representative results are shown in Fig. 8. It can be seen that under the external field, the α (upper) dislocation moves to the right (has moved out of the right boundary and re-entered the left boundary) and the β (lower) dislocation moves to the left. In particular, the α dislocation moves faster than the β dislocation, with a moving distance of ~16 nm for the former as compared to ~5 nm for the latter over the time span shown in Fig. 8. We also find that at the absence of any external electrical fields, dislocations remain stationary.

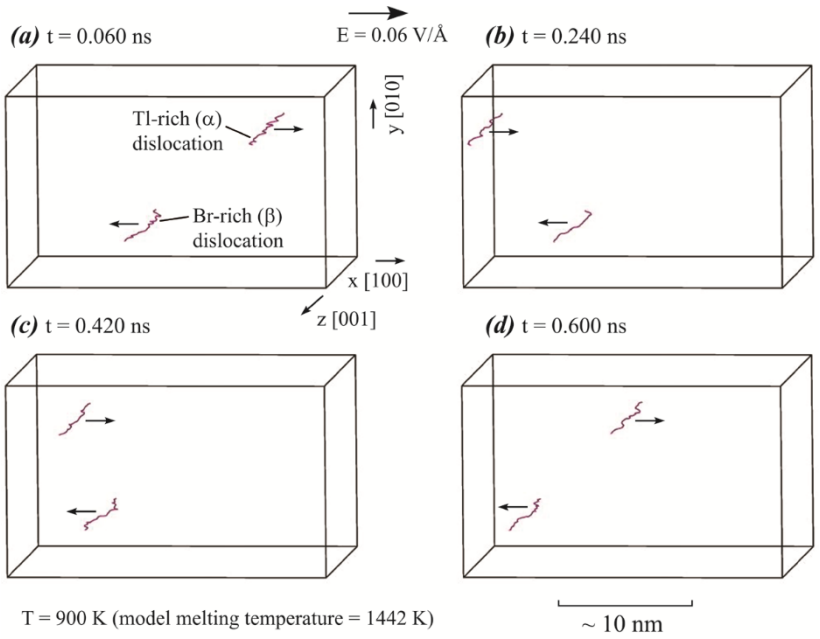

Figure 8. Visualization of dislocation migration under an electrical field.

The successful incorporation of effects of external fields verifies our analytical variable charge model. In addition, the phenomenon observed in Fig. 8 begins to shed new light on the rapid aging of TlBr seen in experiments. This is because the migration of polarized dislocations provides an alternative ionic conduction mechanism not considered previously. Moreover, unlike plastic deformation caused by concerted slip, here dislocation migration is caused by individual jumps of atoms. It is unclear if such dislocation migration can eject other point defects (e.g., vacancies). A full understanding of relationships between dislocation motion and ionic migration induced aging, however, require more extensive simulations under a variety of conditions (e.g., at much longer time scales or using accelerated simulations with elevated temperatures and electrical fields). These will be addressed in the next two Chapters.

*V. **Conclusions***

A simple analytical variable charge model is developed for TlBr. This model reproduces well the quantum mechanical prediction of Born effective charge as a function of lattice strain, and allows MD simulations under an external electrical field. Detailed MD simulations revealed dislocation migration under the field. In particular, α (Tl^+ rich) dislocations move in the

electrical field direction, whereas β (Br^+ rich) dislocations move in the opposite direction, consistent with the sign of their polarizations. α dislocations are also more mobile than β dislocations. Dislocation migration phenomenon should stimulate reconsideration of TlBr aging mechanisms.

4. MOLECULAR DYNAMICS DISCOVERY OF AN EXTRAORDINARY IONIC MIGRATION MECHANISM

I. Abstract

This Chapter will be published as a journal article. In this Chapter, we have applied large scale molecular dynamics simulations to study effects of dislocations on ionic migration of TlBr crystals under electrical fields. We find that electrical fields can drive the motion of edge dislocations in both slip and climb directions. These combined motions eject a large number of vacancies in the dislocation trail. Both dislocation motion and a high vacancy concentration can account for the rapid aging of the TlBr detectors. Our X-ray rocking experiments further confirm the motion of dislocations under electrical fields. These findings suggest that dislocation density and mobility must be reduced before any practical lifetimes of TlBr crystals can be achieved.

II. Introduction

Apparently, the performance degradation of TlBr must be related to the ionic migration, which leads to a build-up of ions at the electrodes thereby counteracting the applied electrical field and impairing the collection of photo induced carriers. Observation of formation of Te-rich dendrites near electrolytes has also provided direct experimental evidence of ionic migration [12]. Interestingly, however, recent studies [19,20,21] indicated that an ionic migration rate that is high enough to account for the rapid aging of TlBr seen in experiments would require a vacancy concentration that is many orders of magnitude higher than the equilibrium vacancy concentration and any excessive vacancy concentrations due to impurities. Therefore, understanding this mysterious, extremely high vacancy concentration becomes critical to guide future efforts to increase the lifetime of the TlBr devices.

Realistic crystals, especially the soft TlBr crystals, always contain a high density of dislocations due to mechanical deformation. It is unclear if dislocations can promote ionic migration. Here we perform large scale molecular dynamics (MD) to study effects of dislocations on ionic migration under external fields. As mentioned in Chapter 2, majority of past MD simulations [24,25,26,27,28,29,30,31] focused on ionic conductivity. As such, the simulations do not apply external electric fields and the systems are simply annealed at sufficiently high temperatures to cause thermally activated diffusion of ions. The diffusion coefficients obtained from the trajectories of ions are then indirectly related to ionic conductivity through Nernst-Einstein equation [74]. Instead, we will apply an external electrical field in MD simulations. Because large systems can be simulated over long time, our studies do not impose any assumptions regarding ionic migration other than introducing dislocations in the system and applying electric fields. As a result, they provide realistic predictions of new phenomena. This is also in contrast to quantum mechanical calculations that are typically used to determine the energetics of a pre-assumed mechanism due to the computational cost.

III. Methods

We apply the TlBr polymorphic potential developed above in molecular dynamics package

LAMMPS [22] to perform our simulations. There is another TlBr potential available in literature [75], but that potential has only been tested for TlBr melt. The advantage of our potential is that it can predict the crystalline growth of the equilibrium phases of both elements and compounds [23], thereby the equilibrium phases are proven to have lower energies than any other configurations that are likely to be sampled due to random adatom addition during the growth simulations. Only potentials with such a validated stability can be used for our simulations because our TlBr crystals must remain stable with respect to any structural disturbance caused by large external electrical fields.

An example of our MD system is showing in Fig. 9. It is a CsCl-type of TlBr crystal containing 60(100) planes in the x direction, 36(010) planes in the y direction, and 56(001) planes in the z direction. Periodic boundary conditions are used in all the three coordinate directions so that the crystal can be viewed as infinitely large. A pair of edge dislocations with a perfect Burgers vector of [100] are created by removing 1(100) plane, or equivalently, 2(200) planes, between a distance d in the y direction. For this work, d is fixed at 18(010) planes. MD simulations are performed at 800 K using an NVT ensemble (constant number of atoms, volume, and temperature) for a total of 2.02 ns. An external electrical field of E = -0.2 V/Å is simulated by applying a biased force of magnitude of |f| = 0.2 eV/Å, to all the Tl atoms in the –x direction and all the Br atoms in the +x direction, assuming a nominal charge of ±1 electron for Tl and Br atoms. To prevent the crystal from shifting during long time simulations, atoms in a small region near the origin point (0,0,0) are fixed.

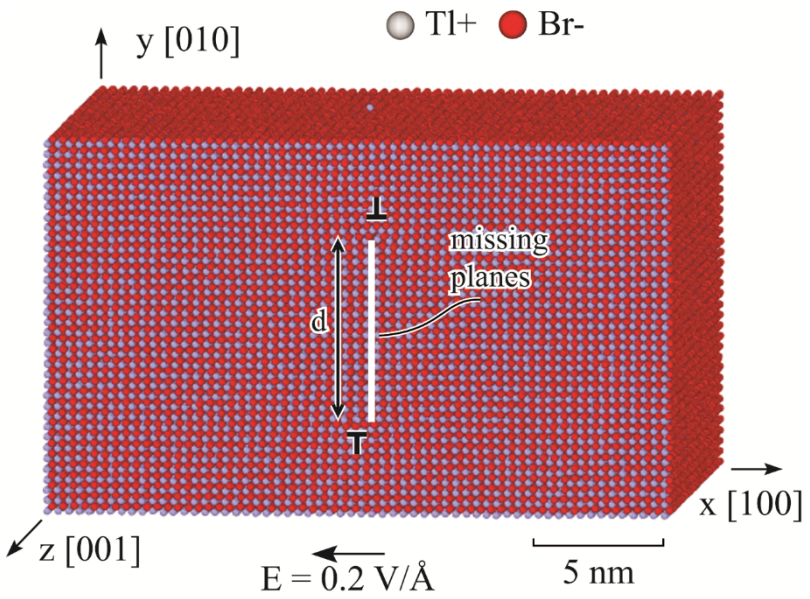

Figure 9. Geometry of TlBr crystals for molecular dynamics simulations under an electrical field.

Our quantum mechanical calculations [67] confirmed that the main effects of external electric fields are to create a biased force in opposite directions to Tl and Br atoms. These forces can be treated independently from the Coulombic interactions between atoms that are already included in the interatomic potential. Most importantly, we found that the biased force remains linearly proportional to the applied field up to an extremely high field of 1.5 V/Å, and the charge derived

from this linear relationship is above the nominal charge ±1 electron. Note that the charge derived from force has been termed Born effective charge [72]. While it is interesting that the Born effective charge is above ±1 electron, assuming the nominal charge would at most miss the simulated field by a factor and it should not impact our goal to reveal mechanisms (rather than to derive quantitative relationships).

*IV. **Results and Discussions***

1. Time Evolution of Dislocation under an Electrical Field

MD configurations obtained at different times are analyzed using the dislocation extraction algorithm developed and incorporated in the visualization software OVITO by Stukowski [73]. We find that at the absence of any external electrical fields, dislocations remain stationary. However, when a sufficiently large electric field is applied and when the temperature is high enough to activate the atomic jumps, dislocations move. As an example, Fig. 10 shows OVITO visualization of dislocations obtained from different times at an electrical field of E = 0.2 V/Å and a temperature of T = 800 K. It can be seen that at the start of simulation, the dislocations are at the original positions as can be confirmed by Fig. 9. At time 0.038 ns, however, the upper dislocation has moved to the left whereas the lower dislocation has moved to the right. With further elapse of time from 0.038 ns to 0.438 ns, Figs. 10(b) – 10(f), the upper dislocation continuously moves to the left. The lower dislocation behaves differently. From 0.038 ns to 0.354 ns, the lower dislocation has moved the entire periodic distance in the right direction, i.e., it has moved out of the right boundary and re-entered from the left boundary before reaching the position shown in Fig. 10(c). Once the lower dislocation reaches the particular location shown in Fig. 10(c), some dislocation segments suddenly change the moving direction, causing the dislocation to bow out. At time 0.370 ns, the left-moving segments win the battle, and the entire dislocation begins to move to the left.

There are additional interesting observations. From 0.370 ns to 0.410 ns, Figs. 10(d) to 10(e), the lower dislocation would have moved the entire periodic distance in the left direction, i.e., the lower dislocation shown in Fig. 10(e) has re-entered from the right boundary. Upon arriving at approximately the same location where the moving direction of the lower dislocation is first reversed, some segments of the dislocation would change the moving direction so that the dislocation bows out as shown in Fig. 10(c). However, the left-moving dislocation segments always win the battle so that eventually the lower dislocation would continuously move to the left, as shown in Figs. 10(e) and 10(f).

In addition to the horizontal motion on the (010) slip plane, the two opposite dislocations are also seen to move vertically in the climb direction. This can be clearly verified in Figs. 10(g) and 10(h), where the two dislocations, which were originally separated in the vertical direction, meet and annihilate.

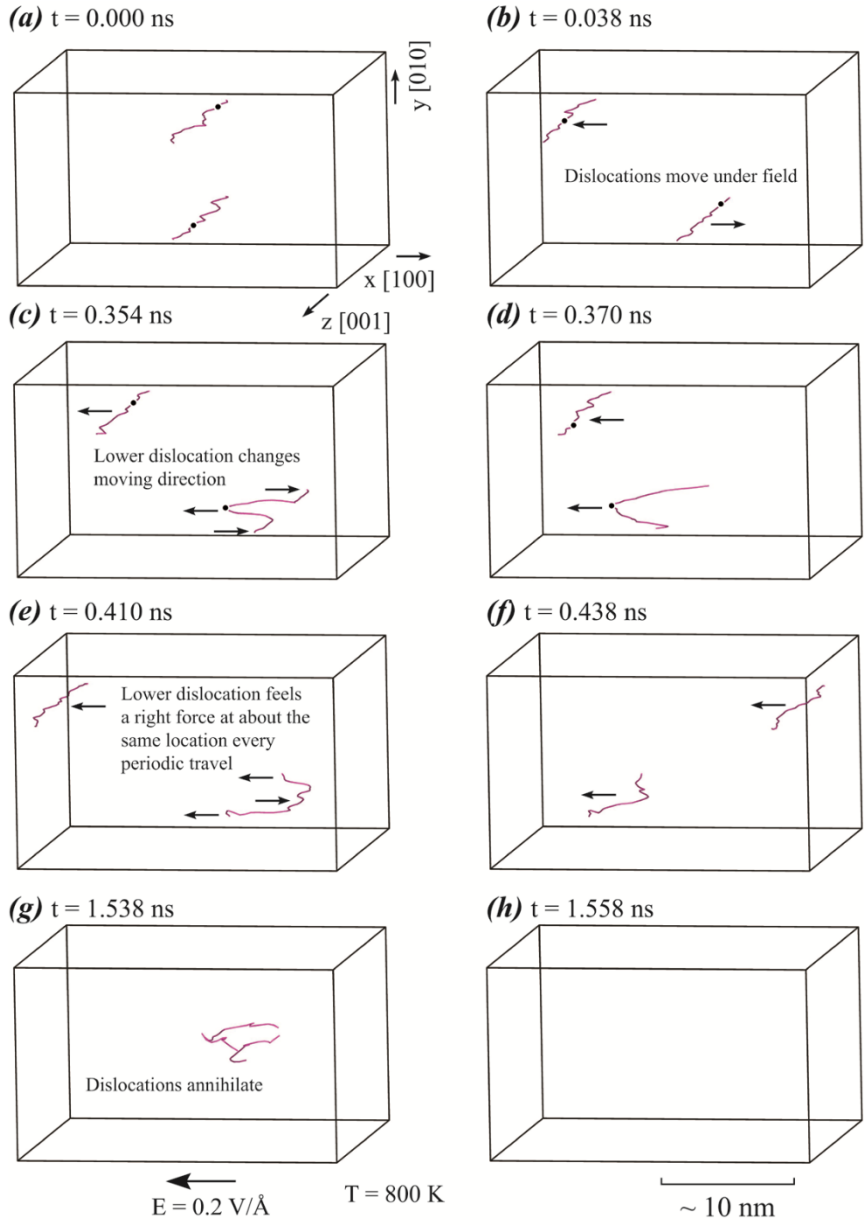

Figure 10. Dislocation vs. time at a temperature of 800 K and an electrical field of 0.2 V/Å. The black dots on the dislocation lines mark the regions where dislocation cores will be further examined in Fig. 11.

The phenomena observed in Fig. 10 are exciting not only because they can account for the rapid ionic migration seen in experiments that cannot been accounted for by the conventional vacancy mechanism, but also because they are truly predicted as we do not impose any assumptions to cause their occurrence. With the phenomena revealed, the following questions arise: Why do dislocations move under electrical fields? Why do the upper and lower dislocations move in opposite directions? Why does the lower dislocation suddenly change the moving direction? Why does the lower dislocation repeatedly encounter opposite forces and therefore bow out at the same location where it first changes the moving direction? Why do dislocations climb and

does the climb requires the migration of point defects? All of these questions will be answered in the following.

2. Dislocation Migration Mechanisms

To understand the motion of dislocations, the core structures of dislocation segments near the regions marked by the black dots in Fig. 10, are examined in Fig. 11. For perfect CsCl-type of crystal structures examined in the orientation of Fig. 11, each lattice unit would contain one atom. It can be seen that dislocations cores can always be identified as the location where an extra atom (in the projected figures) occurs. At time 0.000 ns shown in Fig. 11(a), for instance, the upper dislocation of the top frame has two Tl atoms (marked as "A" and "B") occur within one lattice unit (marked by a black line), and the lower dislocation of the bottom frame have two Br atoms (again "A" and "B") within one lattice unit (line). For convenience, we refer the dislocation with extra Tl atoms at the core to the Tl-rich or α dislocation, and the dislocation with extra Br atoms at the core to the Br-rich or β dislocation. Obviously, dislocation moves only when the leading atoms (marked as "A") at the core make jumps. Under our simulated electrical field, a force in the left direction is applied to the leading Tl atom of the Tl-rich dislocation, and a force in the right direction is applied to the leading Br atom of the Br-rich dislocation. As a result, the Tl-rich dislocations always move to the left and the Br-rich dislocations always move to the right. This mechanism is confirmed by all the configurations we analyzed including those shown in Figs. 11(b) – 11(d). Specifically, the upper dislocation always moves to the left because its core remains to be Tl-rich as shown in Figs. 11(b) – 11(d). On the other hand, when the lower dislocation moves to the right, it has the Br-rich character at the core as seen in Fig. 11(b). Comparison of Figs. 10(c) and 10(d) with Figs. 11(c) and 11(d) indicates that exactly when the lower dislocation changes the direction of motion, its core transforms from a Br-rich configuration to a Tl-rich configuration. Clearly, the charge polarization of dislocation cores is the reason that dislocations in TlBr move under electrical fields, and different polarization ($\pm$) is the reason that different dislocations move in different directions.

To understand why the Br-rich dislocation transforms to the Tl-rich dislocation but not the vice versa, we calculate the core energies of both dislocations. As a relative measure, the core energy E_c is simply defined as the average atomic energy for all the atoms within a radius r_0 from the dislocation core. The results of core energies E_c is plotted as a function of r_0 in Fig. 12 for both dislocations. It can be seen that the Tl-rich dislocation has a lower energy than the Br-rich dislocation over the entire r_0 range explored. This clearly indicates that the Br-rich dislocation is not stable compared to the Tl-rich dislocation. The Br-rich dislocation, therefore, always transforms to a Tl-rich dislocation but not the vice versa.

In order for a dislocation to transform from a Br-rich core to a Tl-rich core, an excess amount of Tl atoms need to be transferred to the core. To understand where these Tl atoms come from, a plan view of two consecutive (010) monolayers adjacent to the slip plane of the lower dislocation right after it changes the moving direction and the core type is examined in Fig. 13. It can be seen that the changes of the dislocation are accompanied by the formation of a large number of Tl vacancies behind the dislocation. This confirms that a Br-rich dislocation transforms to a Tl-rich dislocation when a large number of Tl atoms at the lattice sites jump to the core under the electric field.

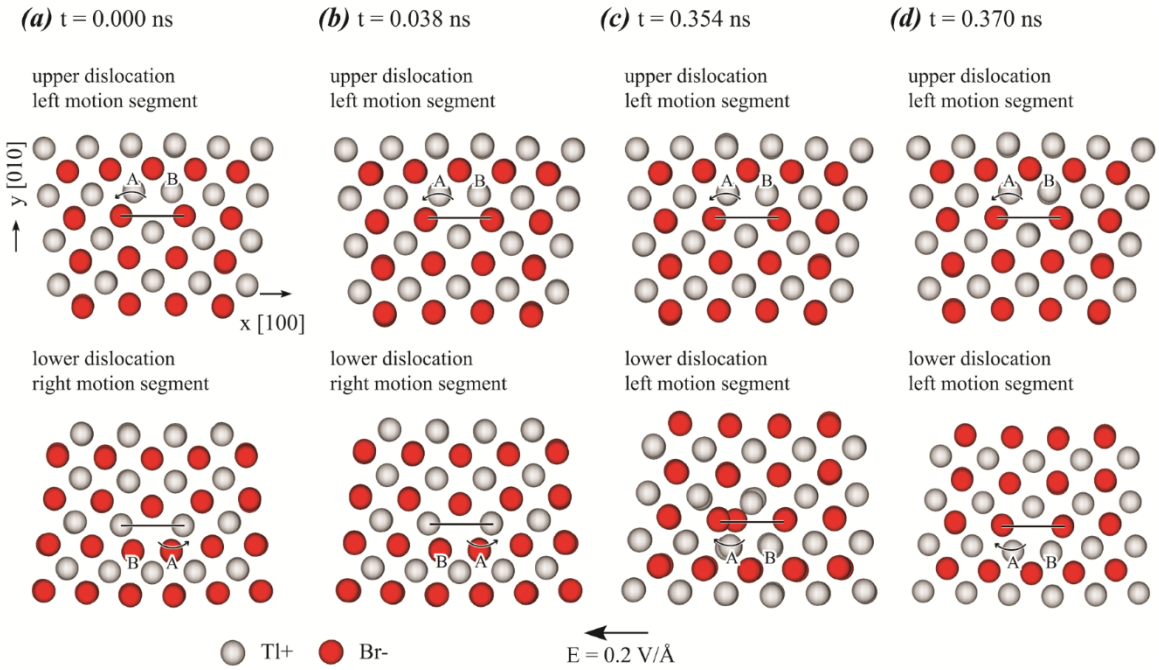

Figure 11. Examination of dislocation cores at various times.

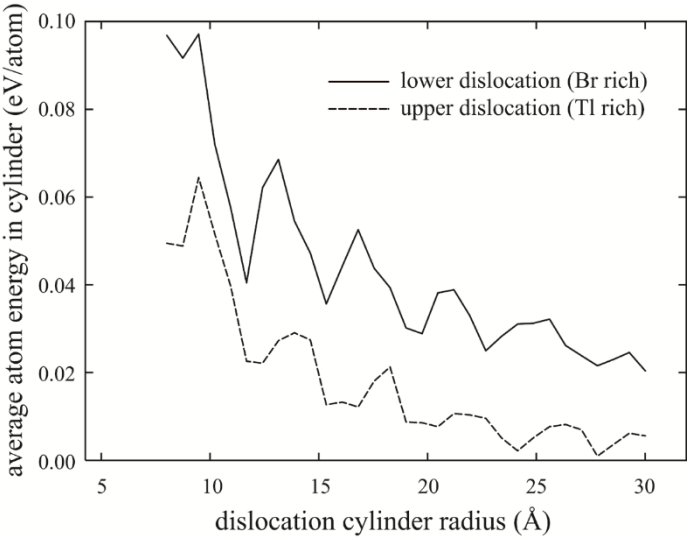

Figure 12. Core energies of Br-rich and Tl-rich dislocations.

Fig. 13 also explains why the lower dislocation encounters an opposite force and bows out every time when it reaches approximately the same location where it first changes the moving direction. This is because this location is associated with a large number of Tl vacancies. When a Tl-rich dislocation comes close, the excess Tl atoms at the core easily fill these vacancies, resulting in a temporary change of the Tl-rich core to a Br-rich core for some of local segments along the dislocation line. The electrostatic forces acting on these segments then change the sign, and the dislocation then bows out to balance the forces on various segments. However, because the Tl-rich dislocation is more stable than the Br-rich dislocation, the Tl atoms on the lattice sites are gradually dragged back to the core. Eventually the entire dislocation becomes Tl-rich again

and therefore continues to move to the left.

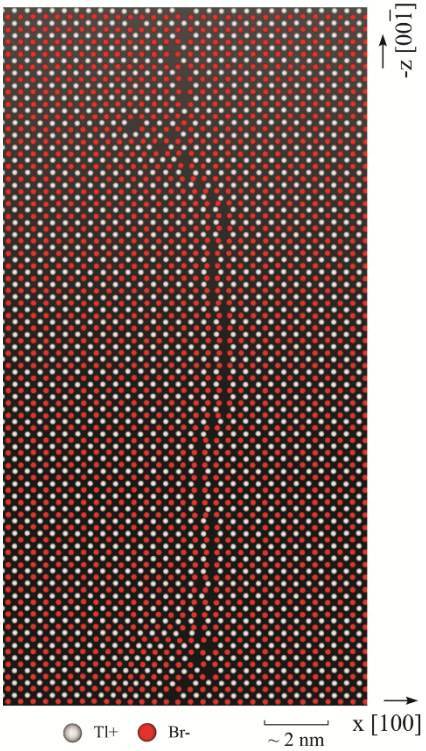

Figure 13. Plan view of two consecutive (010) monolayers adjacent to the slip plane of the lower dislocation after it changes the moving direction. Significant Tl vacancies are observed.

3. Vacancy Generation Mechanisms

Migration of point defects is needed for the climb motion of edge dislocations. Three types of point defects, (Tl and Br) interstitials, (Tl and Br) vacancies, and (Tl at Br and Br at Tl) antisites were analyzed. We found that concentrations of interstitials and antisites are negligibly small (occasionally one or two interstitials or antisites occur out of the entire system containing ~240,000 atoms). However, significant vacancies were observed. Hence, we will focus on vacancies.

In a vacancy-free crystal, each Tl atom should have eight Br neighbors and each Br atom should have eight Tl neighbors. To quantify vacancies, we calculate neighbors of Tl and Br atoms. If a Tl atom has less than eight Br neighbors, this Tl atom is said to have a neighboring Br vacancy. Likewise, if a Br atom has less than eight Tl neighbors, it has a neighboring Tl vacancy. The total number of Tl vacancies is then calculated as 1/8 of the total number of Br atoms that have at least one neighboring Tl vacancy, and the total number of Br vacancies is calculated as 1/8 of the total number of Tl atoms that have at least one neighboring Br vacancy. The factor 1/8 arises because the same, isolated vacancy would have eight atom neighbors. This approach is used to estimate vacancy density (atomic fraction) as a function of time, and the results are shown in Fig. 14.

Fig. 14 shows that vacancy density increases with time until reaches a plateau at around 1.5 to 1.6 ns. Tl ad Br vacancy densities are about the same at all times, satisfying the charge neutrality condition. The time for reaching the plateau coincides exactly with the time when dislocations annihilate, Figs. 10(g) and 10(h). When dislocations annihilate, the missing planes of the edge dislocations "disappear" because all the missing atoms are converted to vacancies. The vacancy density that would match exactly the missing planes is indicated in Fig. 14 using a dash line. It can be seen that our calculated vacancy density is lower than this ideal vacancy density. This is correct because when clustered vacancies are formed, an atom can have more than one vacancy neighbors and a vacancy can have less than eight atom neighbors, both of which cause an underestimate of vacancy density using our method. Nonetheless, the 0.003 vacancy density achieved in Fig. 14, would correspond to a vacancy concentration of ~10^{20} /cm^3, which can sufficiently account for the rapid aging seen in experiments [19,20,21].

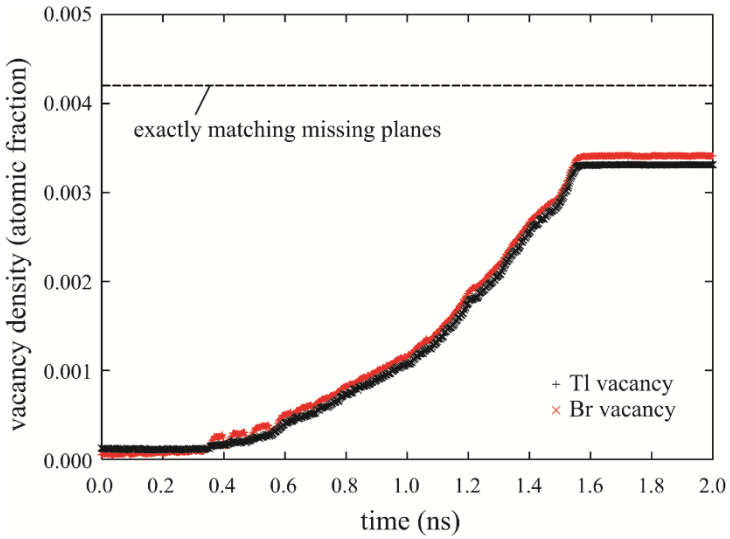

Figure 14. Tl and Br vacancy concentrations as a function of time.

To understand how vacancies are formed, configurations obtained from different times are visualized in Fig. 15, where only atoms with vacancy neighbors are shown along with the location of dislocation core marked by circles. Fig. 15(a) indicates that at time 0.400 ns where dislocations have moved at least a few periodic lengths (see Fig. 10), there are already quite a few Tl and Br vacancies formed in the trail of the dislocations. Fig. 15(b) indicates that at time 1.200 ns, number of vacancies have increased significantly. Interestingly, whereas the two dislocations are seen that have climbed towards each other for quite a distance, vacancy distribution remains to be continuous (at least in the projected figures) up to the location of dislocation cores. This suggests that dislocations continuously eject vacancies as they move. According to the discussion above, the climb motion requires that atoms jump from lattice sites to dislocation cores. Therefore, it is these jumps that cause the formation of vacancies in the dislocation trail.

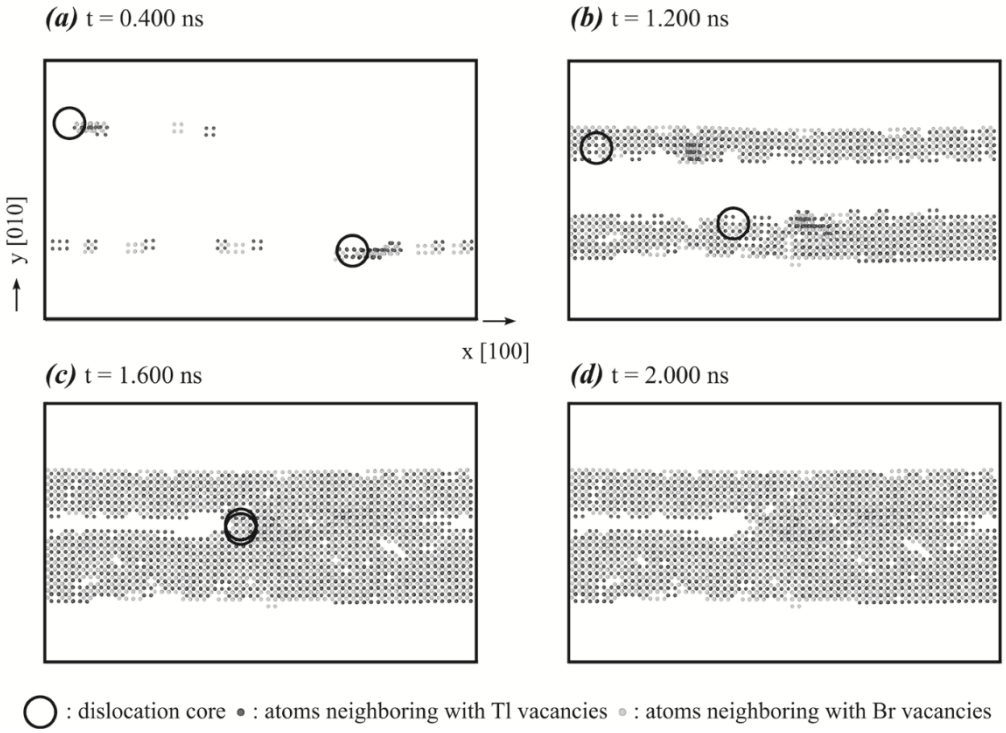

Figure 15. Vacancy formation mechanisms.

The mechanism discussed above is further verified in Figs. 15(c) and 15(d). Fig. 15(c) corresponds to time 1.6 ns. This is when dislocations meet and annihilate as shown in Fig. 10, and vacancy densities reach the plateau as shown in Fig. 14. It can be seen that vacancies are present all the way to the location of dislocation annihilation. Once dislocations are annihilated, no more vacancies are created with a further increase of time to 2.000 ns, Fig. 15(d). Clearly, vacancies are formed due to the climb motion of dislocations.

V. ***Experimental Validation***

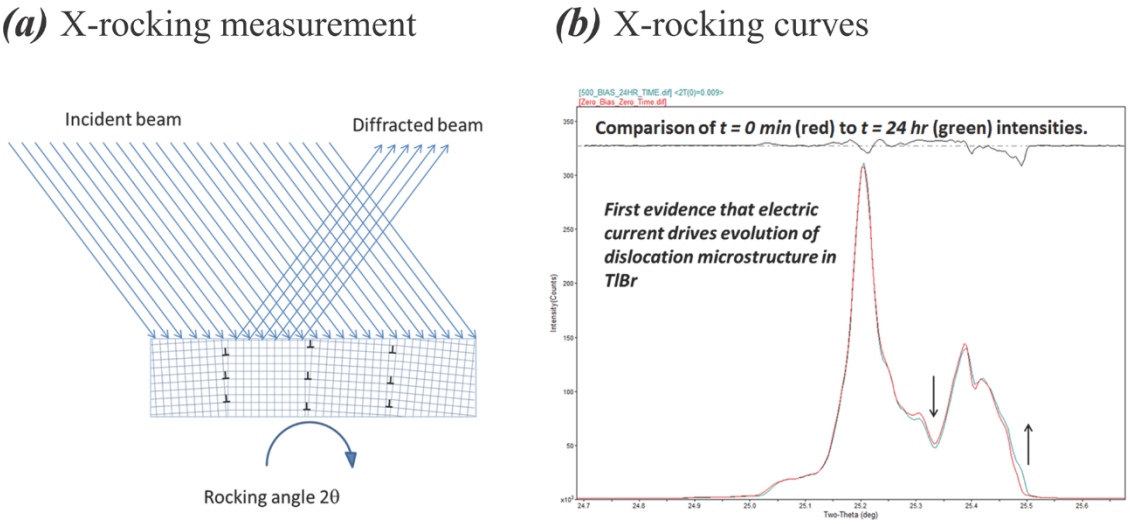

Figure 16. (a) schematic of X-rocking experiments; and (b) X-rocking curves.

X-rocking experiments shown in Fig. 16(a) are performed to study dislocation structures of the melt-grown TlBr samples, and the results are shown in Fig. 16(b). The TlBr samples are found to have a high-temperature dislocation microstructure consisting of dislocation "walls" or subgrain boundaries. X-ray rocking curves reveal the relative orientations and sizes of these domains as they rock through the diffracting condition. In particular, Fig. 16(b) shows monotonic changes in the relative intensities during room-temperature application of electric fields, showing that the dislocations migrate under device operating conditions. This validates the simulated results that dislocations move under electrical fields.

VI. ***Conclusions***

Large scale molecular dynamics simulations have been performed to simulate the effects of dislocations on ionic migration of TlBr crystals under external electrical fields. We found that due to the ± polarizations of the dislocation cores, Tl-rich (α) and Br-rich (β) dislocations move in opposite dislocations under a large electrical field. Unlike mechanical deformation induced dislocation motion that is constrained on the slip plane, the electrical field induced dislocation can move in both slip and climb directions. Due to the climb motion, dislocations eject a large number of vacancies in their trails. The concentrations of such vacancies can be many orders of magnitude higher than the equilibrium vacancy concentration or impurity induced vacancy concentration. Dislocation motion under electrical fields has been validated by our X-rocking experiments. Hence, our work indicates that reducing dislocation density and strengthening materials (reducing dislocation mobility) may be an effective strategy to reduce the aging of the materials. Despite extensive studies and enormous interests, past efforts to extend lifetimes of TlBr have not considered dislocations.

5. MOLECULAR DYNAMICS "DEVELOPMENT" OF AGING RESISTANT TLBR CRYSTALS

I. Abstract

This Chapter will be published as a journal article. The molecular dynamics simulations and X-ray rocking experiments discussed in Chapter 4 have shown that electrical fields can drive the motion of edge dislocations in both slip and climb directions. These combined motions eject a large number of vacancies. Both dislocation motion and vacancy ejection can account for the rapid aging of the TlBr detectors. Based on these new discoveries, the present Chapter applies molecular dynamics simulations to "develop" aging-resistant TlBr crystals by inhibiting dislocation migration under electrical fields.

II. Introduction

As stated above, performance degradation must be related to ionic migration. On the other hand, quantum mechanical calculations [19,20,21] indicated that an ionic migration rate that is high enough to account for the rapid aging of TlBr seen in experiments would require a vacancy concentration that is many orders of magnitude higher than the equilibrium vacancy concentration and any excessive vacancy concentrations due to impurities. In Chapter 4, we performed large scale molecular dynamics (MD) simulations and X-ray rocking experiments on dislocation evolution under external electrical fields [67,76]. We found that external electrical fields can drive the motion of edge dislocations in both slip and climb directions. These combined motions eject a large number of vacancies in the dislocation trail. Both dislocation motion and a high vacancy concentration can cause the rapid aging of the TlBr detectors. Based on these discoveries, one approach that can potentially solve the aging problem would be to strengthen TlBr so that dislocations no longer move under electrical fields. With this recognition, the present work uses MD simulations to "develop" aging resistant TlBr crystals by exploiting the orientation hardening* and the precipitate hardening effects.

III. Methods

Similar to Chapter 4 [67], we apply the TlBr polymorphic potential [23] in the molecular dynamics package LAMMPS [22] to perform simulations. The external electrical field is modeled by applying opposite forces to Tl and Br atoms in the field direction. The magnitude of the force equals the product of the magnitude of field and the nominal charges of ±1 e. To model an AB precipitate, we simply assume that A is a variant of Tl and B is a variant of Br except that the total energy expression is multiplied (strengthened) by a factor of 1.2 and no electrostatic forces are applied to A and B atoms during simulations. The resulting AB compound is therefore stiffer and non-ionic.

Our simulations employ a CsCl-type of TlBr crystal containing 60(100) planes in the x direction, 36(010) planes in the y direction, and 56(001) planes in the z direction. Periodic boundary

* By the orientation strengthening, we mean that the resolved electrostatic force of the external electrical field in the Burgers vector direction can be reduced by changing the crystallographic orientation.

conditions are used in all the three coordinate directions so that the crystal can be viewed as infinitely large. An edge type of dislocation dipole with the typical Burgers vector of <100>a is created by first removing one {100} plane, or equivalently, two {200} planes, between a distance d, and then ramping the neighboring atoms to close the gap. Examples of the dislocation configurations are shown in Figs. 17(a)-17(c), where in Figs. 17(a) and 17(c), the dislocation dipole is along the y[010] direction whereas in Fig. 17(b), the dislocation dipole is along the x[100] direction. Note that Figs 17(a) and 17(b) do not contain precipitates. Fig. 17(c) contains two AB precipitates of the same CsCl crystal type with 5×5 unit cells on the x-y plane and a full periodic length in the z direction. To clearly show the AB precipitates, Tl and Br atoms are made transparent in Fig. 17(c). When the crystal geometry is given as shown in Figs. 17(a)-17(c), two electrical field directions, [100] and [111], are applied as shown in Fig. 17(d). For comparison, we also further assume that the dislocation dipole distance d is fixed at 18(010) planes.

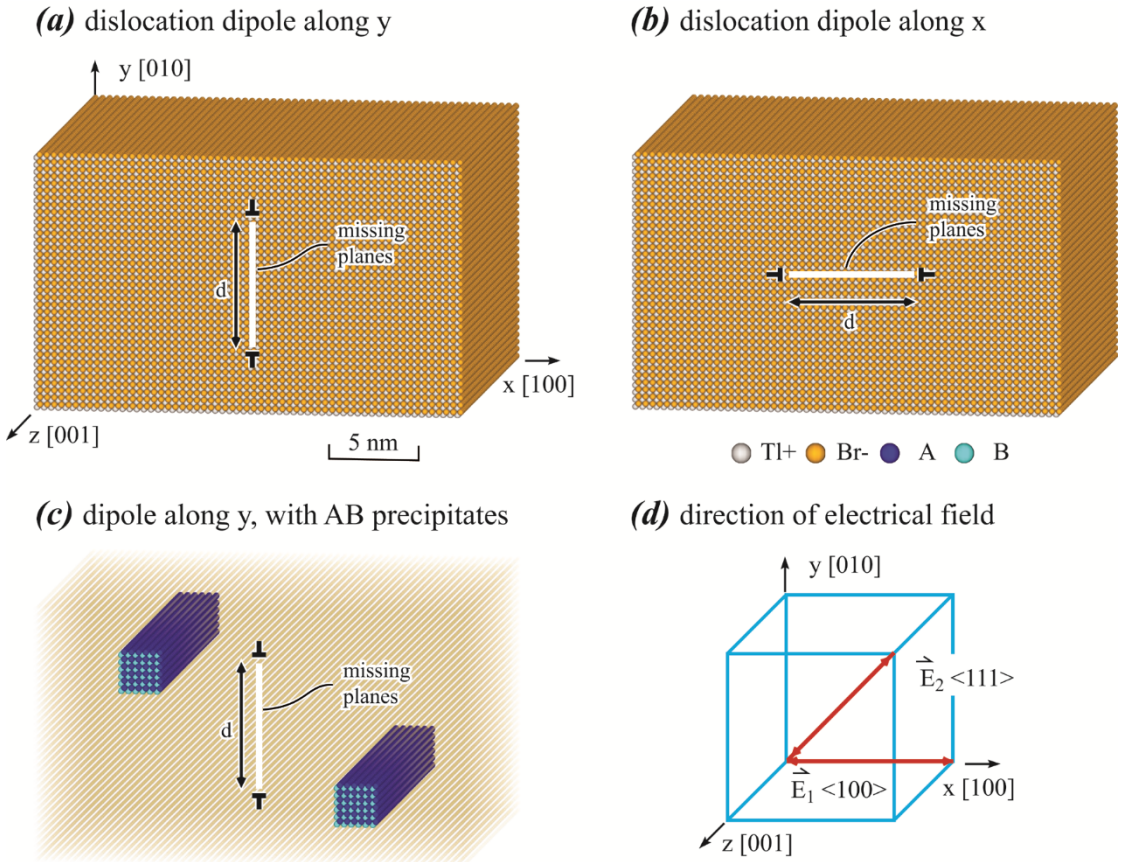

Figure 17. Molecular dynamics models: Dislocation dipole along (a) y[010] and (b) x[100] directions without precipitates; (c) dislocation dipole along y[010] direction with precipitates; and (d) schematic of electrical field directions.

Four scenarios are considered: (i) applying a [$\bar{1}$00] field to Fig. 17(a), i.e., the field is parallel to the Burgers vector; (ii) applying a [$\bar{1}$00] field to Fig. 17(b), i.e., the field is perpendicular to the Burgers vector; (iii) applying a [$\bar{1}\bar{1}\bar{1}$] field to Fig. 17(a), i.e., the angle θ between the field and the Burgers vector satisfies $\cos\theta = 1/\sqrt{3}$; and (iv) applying a [$\bar{1}$00] field to Fig. 17(c). Comparison of scenarios (i)-(iii) fully reveals the orientation strengthening effects, and comparison of scenarios

(i) and (iv) fully reveals the precipitate hardening effects.

For each of the four scenarios described above, two MD simulations are performed for a total of 2.0 ns at two electrical fields of |E| = 0.1 V/Å and E| = 0.2 V/Å and one fixed temperature of 800 K using an NVT (constant number of atoms, volume, and temperature) ensemble[†]. To prevent the crystal from shifting during long time simulations, atoms in a small region near the origin point (0,0,0) are fixed.

*IV. **Results***

1. Time Evolution of Dislocation under the High Electrical Field of |E| = 0.2 V/Å

The work performed in Chapter 4 is essentially the same as scenario (i) at the field of |E| = 0.2 V/Å. To facilitate the current discussions, the previous findings are first summarized: Upon the application of the external field pointing to the left, the upper dislocation moved to the left, and the lower dislocation moved to the right initially. This is because the upper dislocation is of the α type with excess Tl+ ions at the core, and the lower dislocation is of the β type with excess Br- ions at the core. However, after the upper dislocation swept the entire periodic length, the lower dislocation transformed also to an α dislocation and began to move to the left at the same average velocity as the upper dislocation. The reason that dislocation transformed from β to α, but not from α to β, is because α dislocations have lower energies. As dislocation moved in the horizontal direction, they also climbed towards each other in the vertical direction by ejecting a large number of vacancies behind.

Returning to the present work, dislocation configurations are analyzed using the dislocation extraction algorithm developed and incorporated in the visualization software OVITO by Stukowski [73]. The results of dislocation configurations at two different times of t = 0.04 ns and t = 2.0 ns are compared in Figs. 18(a)-18(d) for the four scenarios under the high field of |E| = 0.2 V/Å. Here, the dislocation is contrasted in gray in Figs. 18(a) – 18(c) and in purple in Fig. 18(d). Note that the vertical lines in the left frames mark initial locations of some selected atoms. For scenario (i) where the field direction aligns with the Burgers vector, we find exactly the same dislocation migration process as reported in Chapter 4. For example, the lower dislocation initially moves to the right and then moves to the left. Overall, both dislocations move a long distance to the left during the 1.96 ns time span as can be seen from Fig. 18(a). In particular, the middle portion of the marker is seen to move to the right by a distance 29a where a is lattice constant. This means that both top and bottom dislocations have swept the entire x dimension of the periodic cell 29 times. The top and bottom portions of the marker are not seen to move. This is expected because these portion are connected to the small fixed region near the origin point (0,0,0). Considering that the x dimension is about 24 nm, dislocations have moved a total distance of about 0.696 μm over the 1.96 ns time span, giving rise to a dislocation velocity of about 350 nm/ns. In addition to the horizontal motion on the (010) slip plane, the two opposite dislocations are also seen to move vertically in the climb direction as compared to their original

[†] The temperature damping coefficient used in the present Chapter is 0.1 ps as opposed to 100.0 ps in the Chapter 4 [76], and as a result, the precise dislocation dynamics may slightly differ.

locations indicated by the horizontal dash lines. This confirms that the 0.2 V/Å electrical field can cause dislocation motion and vacancy ejection, as reported in Chapter 4.

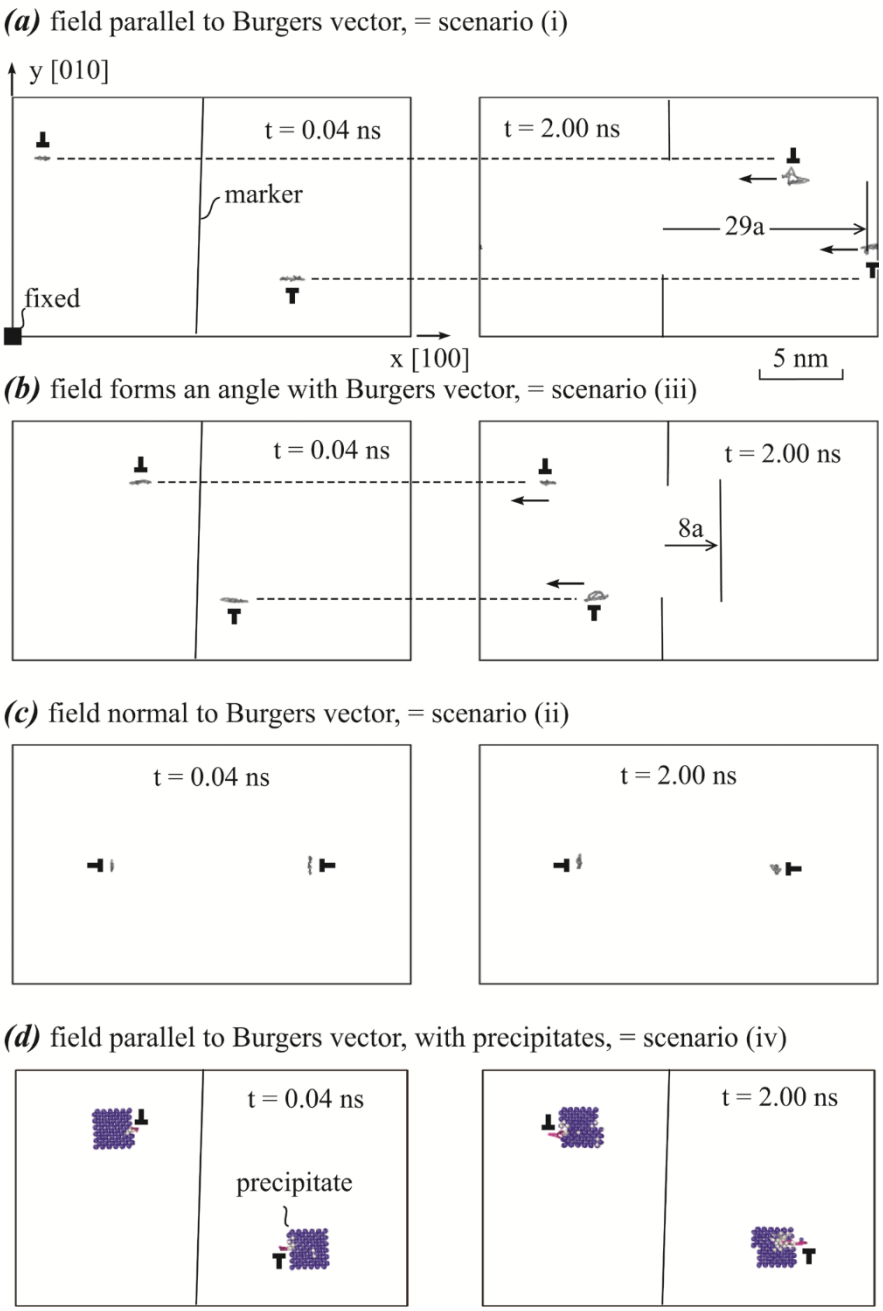

Figure 18. Dislocation vs. time at a temperature of 800 K and an electrical field of 0.2 V/Å: (a) field parallel to Burgers vector, i.e., scenario (ii); (b) field forms an angle with Burgers vector, i.e., scenario (iii); (c) field normal to Burgers vector, i.e., scenario (ii); and (d) field parallel to Burgers vector with precipitates, i.e., scenario (iv).

The same process is also observed for scenario (iii) shown in Fig. 18(b) where the 0.2 V/Å filed is applied in the [111] direction. However, because the field direction forms an angle of $\theta \approx 55^{o}$

with the [100] Burgers vector, the resolved electrostatic force in the Burgers vector direction is reduced. As a result, the left motion of dislocations is much slower. In particular, the middle portion of the marker only moves to the right by 8a, meaning that the dislocations only sweep the periodic length 8 times over the 1.96 ns span. This translates to an average dislocation velocity of about 95 nm/ns. More importantly, no appreciable dislocation climb can be found in Fig. 18(b).

Fig. 18(c) shows that when the 0.2 V/Å field is applied in a direction perpendicular to the Burgers vector as for scenario (ii), dislocations never move over the 1.96 ns time span. This is expected because there was no resolved electrostatic force to drive atom shift in the Burgers vector direction. Because dislocation motion can be effectively reduced, Figs. 18(a)-18(c) convincingly demonstrate that the orientation hardening effect can extend the lifetime of TlBr detectors.

Using the worst case scenario where the 0.2 V/Å field is parallel to the Burgers vector as in Fig. 18(a), we now examine the effects of precipitates. The situation considered is equivalent to scenario (iv), and the corresponding dislocation evolution from t = 0.04 ns to t = 2.0 ns is shown in Fig. 18(d). Considering that both dislocations are in the middle at the start of simulation (t = 0) as shown in Fig. 17(a), Fig. 18(d) means that the lower dislocation moves to the right (initially) and the upper dislocation moves to the left until they both encountered precipitates at t = 0.04 ns. With further elapse in time to t = 2.0 ns, these dislocations are seen to have cut through the precipitates. As established above, the lower dislocation would begin to move to the left after initial motion to the right. However, this left motion is blocked by the precipitate. Because the lower dislocation cannot move to the left, it imposes stresses to the trailing upper dislocation (periodic image) so that the upper dislocation cannot move to the left either. As a result, both dislocations are arrested by the precipitates. All of these are clearly shown by comparing the left and the right frames of Fig. 18(d). Note that no dislocations sweep the periodic length because the marker remained intact.

A top view of the right frame of Fig. 18(d) is further examined in Fig. 19. It can be seen that significant portions of dislocations are arrested inside the precipitate, especially for the lower dislocation. Dislocation segments that are inside the precipitates are charge neutral and are not subject to the electrostatic force. Dislocation segments that are at the precipitate/matric boundary are subject to a lower electrostatic force. Hence, non-ionic precipitates can inhibit dislocation motion. Figs. 18(a) and 18(d) therefore convincingly demonstrate that the precipitate hardening effect can extend the lifetime of TlBr detectors.

Fig. 18(c) has shown that when the field $\vec{E}$ is perpendicular to Burgers vector $\vec{b}$, for example, $\vec{E}$//[100], and $\vec{b}$//[010], dislocation motion can be completely inhibited. Practically, this can never be achieved because Burgers vectors in TlBr are <100>, so any field direction from the <100> series will be parallel to some Burgers vectors. A practical approach will be to use the <111> field direction which is not parallel to any Burgers vectors. Fig. 18(b) shows that the <111> field direction can slow the dislocation motion. To induce dislocation motion within the short MD time scale, the magnitude of the electrical field used in our simulations is orders of magnitude higher than those used in experiments. It is therefore possible that the use of the <111> field direction can completely inhibit dislocation motion at a lower field. To explore this, Figs. 20(a) and 20(b) compare the effects of field direction at a reduced field of |E| = 0.1 V/Å.

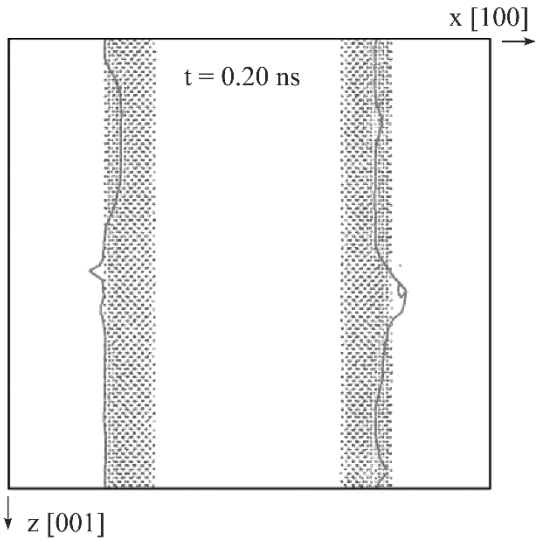

Figure 19. Top view of the right frame of Fig. 18(d).

2. Time Evolution of Dislocation under the Low Electrical Field of |E| = 0.1 V/Å

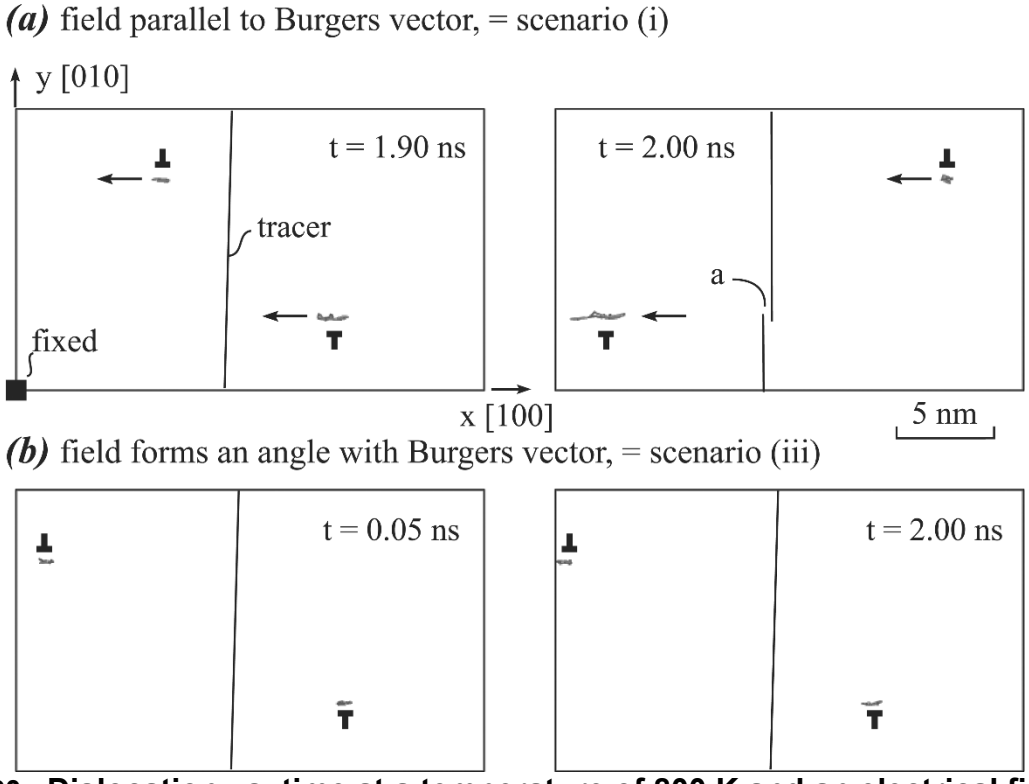

Figure 20. Dislocation vs. time at a temperature of 800 K and an electrical field of 0.1 V/Å: (a) field parallel to Burgers vector, i.e., scenario (i); and (b) field forms an angle with Burgers vector, i.e., scenario (iii).

Fig. 20(a) shows that when the field was parallel to the Burgers vector, dislocation could still move rapidly. In particular, the dislocations had moved by more than half of the periodic length

within a time span of only 0.1 ns. During this motion, the lower dislocation cut through the marker, leaving a one lattice constant step on the marker line. This translates to a dislocation velocity of slightly higher than 120 nm/ns. In sharp contrast, Fig. 20(b) indicates that the dislocations with the [100] Burgers vector did not move over a much longer time span (from t = 0.05 ns to t = 2.0 ns) when the [111] field direction is applied. It is likely that the orientation strengthening effect can also completely shut down dislocation motion in realistic conditions.

3. Vacancy Generation Mechanisms

Fig. 18(a) shows the climb motion of dislocations, suggesting the ejection of vacancies. To quantify this effect, vacancy concentrations (atomic fractions) are calculated as a function of time for all the four scenarios shown in Fig. 18 using the same algorithm as described in the Chapter 4 [76]. The results obtained for the high field of |E| = 0.2 V/Å are shown in Fig. 21.

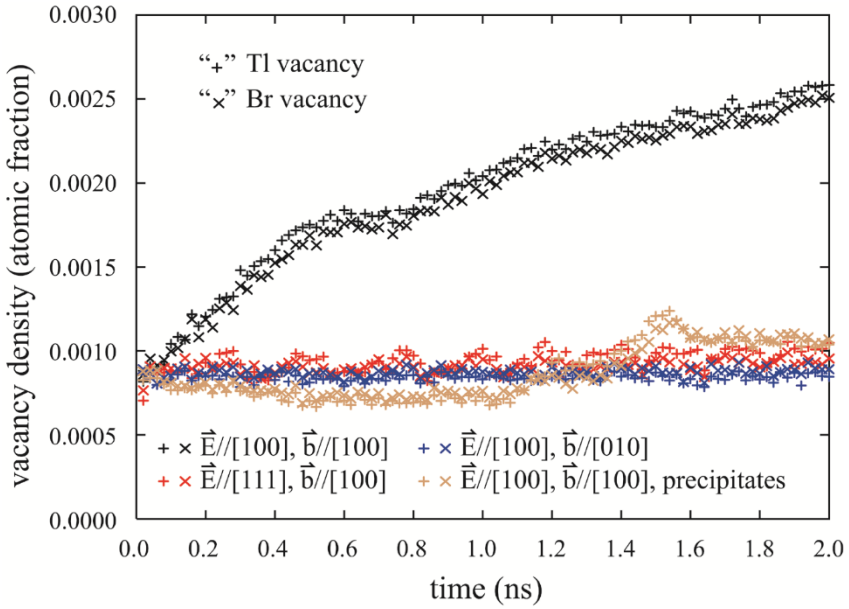

Figure 21. Tl and Br vacancy concentrations as a function of time for all four scenarios at the high field of |E| = 0.2 V/Å.

Fig. 21 indicates that when the field aligned with the Burgers vector, vacancy concentration increased with time. This is consistent with continuous dislocation climb seen in Fig. 18(a). In sharp contrast, when the orientation hardening (whether the field is ideally perpendicular to or forms an angle with the Burger vector) or the precipitate hardening approach was applied, no clear increase of vacancy concentration with time can be identified. This is also consistent with the lack of dislocation climb in Figs. 18(b)-18(d). On the other hand, there are some finite vacancy concentrations in the samples with orientation and precipitate hardening treatment. This is because dislocation core can be identified as a row of vacancies in our algorithm. In addition, the reversal of the moving direction of the lower dislocation is accompanied by the transformation of the β dislocation to α dislocation, which also creates some vacancies as seen in Chapter 4 [76].

To further understand the vacancy formation mechanisms, configurations obtained at different

times are visualized in Fig. 22 for selected cases under the 0.2 V/Å field, where only atoms with vacancy neighbors are shown along with the location of dislocation core marked by circles. Fig. 22(a) indicates that when the field is parallel to the Burgers vector, a large number of Tl and Br vacancies (notated as V_{Tl} and V_{Br} respectively) are continuously ejected in the dislocation trail. This is consistent with Fig. 21 where vacancy concentrations continuously increase with time, and with Fig. 18(a) which shows dislocation climb. Fig. 22(b) indicates that when the field forms an angle with the Burgers vector, the motion of the upper dislocation does not create vacancies because the few vacancies seen in the upper part of Fig. 22(b) represent only the dislocation core. The lower dislocation creates some vacancies but these vacancies are not caused by dislocation motion but are rather caused by the β to α dislocation core transformation.

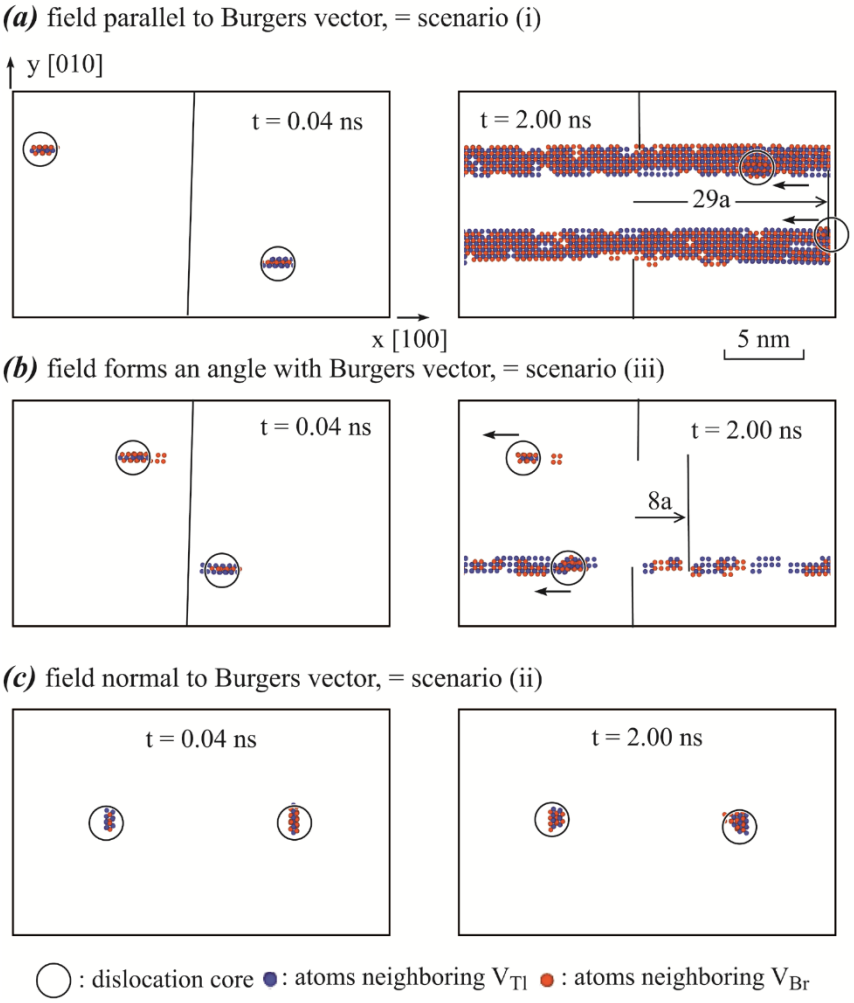

Figure 22. Vacancy configuration vs. time at a temperature of 800 K and an electrical field of 0.2 V/Å: (a) field parallel to Burgers vector, i.e., scenario (i); (b) field forms an angle with Burgers vector, i.e., scenario (iii); and (c) field perpendicular to Burgers vector, i.e., scenario (ii).

Fig. 22(c) indicates that when the field is perpendicular to the Burgers vector, neither vacancy formation nor dislocation climb occurs. This is interesting because the external field aligns with the dislocation climb direction which appears to facilitate the climb and vacancy formation. Fig.

22(c) therefore strongly indicates that dislocation motion on the slip plane is a necessary condition for dislocation climb motion and the related vacancy formation. Clearly, orientation and precipitate hardening reduces the dislocation motion and therefore the vacancy concentration, which in turn extends the lifetime of TlBr detector.

V. ***Conclusions***

Chapter 4 indicates that external electrical field can drive the motion of dislocations in both slip and climb directions. The climb motion ejects a large number of vacancies. In this Chapter, molecular dynamics simulations have been performed to study the orientation and the precipitate hardening effects on dislocation migration. We find that dislocation velocity can be reduced by misaligning the external field with the Burgers vector, or by creating non-ionic stiff precipitates. When dislocation velocity is reduced below a threshold, the climb motion and vacancy formation can be completely eliminated. Hence, we predict that the lifetime of TlBr detectors can be extended by strengthening the material. The orientation and the precipitate strengthening methods are just two examples that are shown to reduce aging in our MD simulations.

This page is intentionally left blank.

6. TECHNOLOGY ADVANCE: THALLIUM BROMIDE (TLBR) SEMICONDUCTORS WITH EXTENDED LIFE

I. Abstract

This project has resulted to an invention (Sandia Disclosure #14052) to extend the life of TlBr crystals and devices. TlBr has electronic properties needed for room temperature gamma ray spectrometers; however, the properties degrade rapidly under electric fields required for this application. The accepted mechanism for this aging, the field-induced motion of charged point defects (vacancies), is clearly incomplete, since quantum mechanical calculations indicate these defects must be present far in excess of their equilibrium concentrations [19,20,21]. Our molecular dynamics simulations reveal that electric fields drive the motion of extended defects (edge dislocations), which generates large concentrations of vacancies. Hence, aging is dramatically accelerated by field-induced motion of dislocations. The significance of this finding is that the useful life of TlBr crystals and detectors can be extended by controlling: (a) resolved electromotive forces on mobile defects; (b) the defect densities; and (c) the defect mobilities.

II. Invention

Thallium bromide is a wide bandgap, high atomic number semiconductor, making it a suitable candidate for efficient gamma ray detection and spectroscopy. The principal advantages over commercially available CdZnTe (CZT) are higher atomic number (1 cm thick TlBr has photoelectric absorption equivalent to more than 1.6 cm of CZT at the benchmark gamma energy of 662 keV), and wider bandgap (potentially reducing dark current, and enabling low noise detectors with greater thickness). These advantages could lead to gamma spectrometers with order of magnitude higher photopeak efficiency than has been achieved in CZT.

While TlBr was one of the first compounds identified as a viable semiconductor for nuclear detectors [77], poor charge collection and rapid aging has hindered development of practical devices for decades. But recent work on purification, crystal growth, and device processing has renewed interest in developing high performance gamma spectrometers in this material. Research at the Tohoku Institute of Technology showed that extensive zone refining can improve the charge transport figure of merit in TlBr crystals [78,79,80], demonstrating a clear correlation between purity and the mobility-lifetime products for electrons and holes. University of Helsinki researchers identified improved crystal quality with purification [81], hydrothermal annealing [82] , and detector manufacturing processes [83,84]. Investigations at the Brazilian Nuclear and Energy Research Institute (IPEN/CNEN) on surface processing and vacuum annealing [15], and crystalline defects and impurities [85,86], showed that controlling these factors improved detector performance. These and other studies show that TlBr detector performance is highly sensitive to the material purity and structural perfection, and is therefore not necessarily limited by fundamental material properties. The improved material quality is reported to correlate with somewhat reduced rates of aging in TlBr devices. Despite these gains, the longest observed stable room temperature operation is still on the scale of months [1,2,21]. Aging in TlBr devices is characterized by a space charge polarization effect (accumulation or depletion of charge under one or both contacts), and chemical reactions, causing corrosion of contact metals, and reduction of Tl+ matrix ions to metallic thallium at the cathode. These effects are understood qualitatively

to be driven by electro-migration of thermal and/or impurity-generated cation and anion vacancies; however quantitative first principles modeling does not support this mechanism alone for the rapid rate of these aging effects. Researchers at Lawrence Livermore National Laboratory investigated ionic mobility in TlBr and its possible association with the polarization effect using parameter-free quantum simulations [21]. The results indicate that neither background impurity ions nor vacancies generated in thermal equilibrium concentrations can traverse distances large enough to generate observed zones of accumulation and depletion in the crystal.

Based on the simulations described in previous Chapters, our project on aging of TlBr reveals a previously unknown mechanism for vacancy generation, which accounts for the observed rates of degradation [67]. Our simulations are based on a new hybrid interatomic potential model coupled with a variable ionic charge model parameterized by first principles. This approach enabled the first molecular dynamic simulations of intrinsic defects in TlBr drifting under an applied electric field. Assembled from Figs. 10, 11, 14, and 15, Fig. 23 summarizes the results.

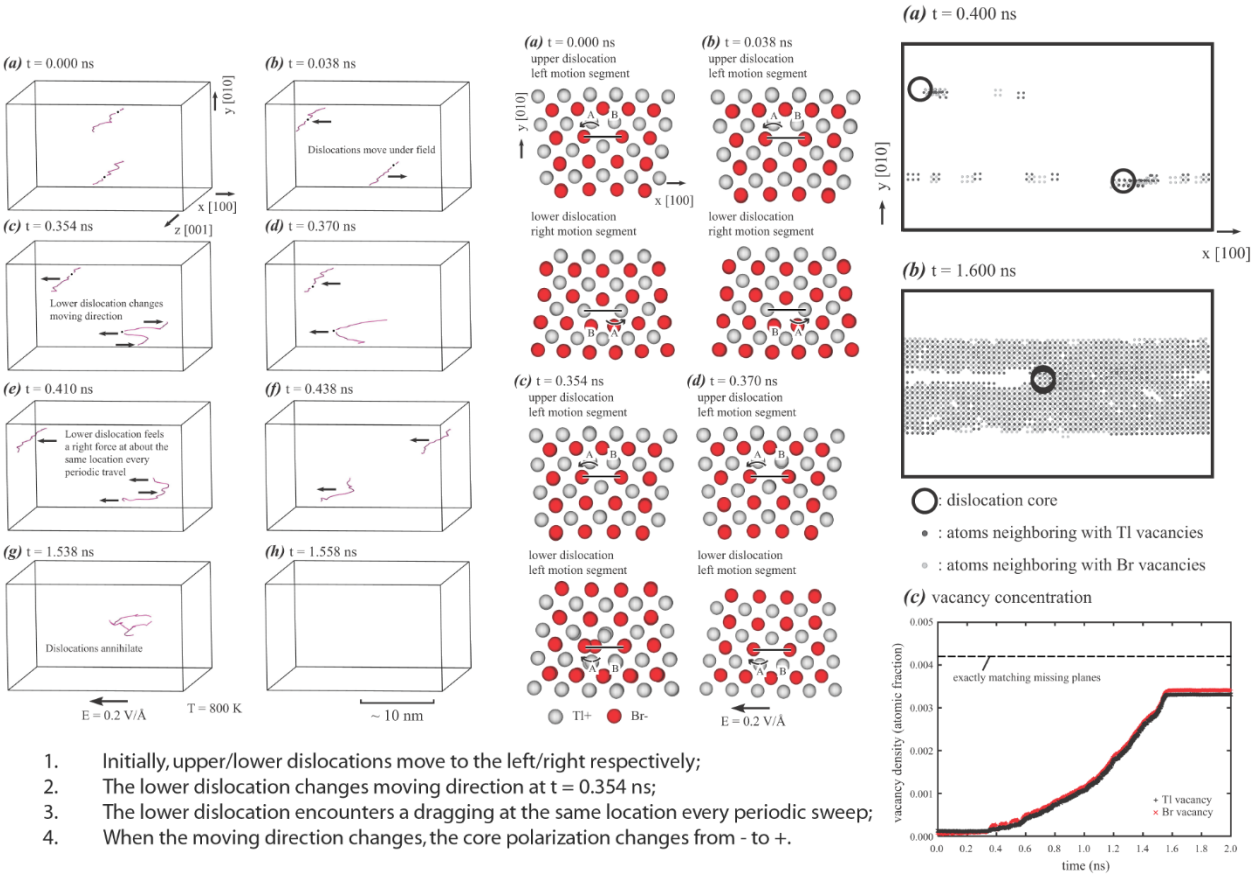

Figure 23. Simulations reveal that previoulsy neglected dislocations can be driven by electric fields. This forced motion of dislocations in TlBr causes abundant vacancy production, far in excess of thermal or chemical equilibrium.

The left series of images of Fig. 23 shows a time sequence of dislocation lines moving under the influence of an applied electric field. The movements are at first similar to typical low temperature "glide" motion caused by mechanical stresses. However as shown in (g) of the left panel, unlike mechanical stress alone, the electric field induces "climb" motion (and dislocation

annihilation) as well, resulting in production of vacancies. These vacancies are visualized using a bond counting algorithm in the right panel of Fig. 23.

Elucidation of the heretofore neglected effects of dislocations on aging in TlBr opens a large number of unexplored avenues to improve the material and device designs for extended life. These new approaches, centering on controlling dislocations, are summarized below (note that the approaches highlighted in yellow have been in fact confirmed by MD simulations as described in Chapter 5):

1. **Reducing resolved electromotive force**
   i. Crystallographic orientation
   ii. Device geometry
      a) Shape (planar, trapezoidal, hemispherical)
      b) 3D contact structures

2. **Reducing dislocation mobility**
   i. Bulk
      a) Isovalent alloys
      b) Aliovalent alloys
      c) Particle strengthening
      d) Work hardening
   ii. Contact region
      a) Alloy, soluble ion implantation
      b) Particle, insoluble ion implantation
      c) Ion beam damage

3. **Reducing Dislocation density**
   i. Bulk
      a) Reduced wall effect (e.g. CZ, float zone, horizontal Bridgman)
      b) Bulk growth (particle or alloy strengthening)
   ii. Contact region
      a) Multilayers (SLS, etc.)
      b) Heterojunctions (TlCl, HgI2, MAPbBr3, etc.)
      c) Engineered voids (terminate dislocation subsurface)
      d) Epitaxial buffer layers, (> critical thickness)

4. **Creating polycrystalline layers (homo or hetero layers)**

Distribution

1. MS0958	Pin Yang	Org. 1816
2. MS1349	Hongyou Fan	Org. 1815
3. MS1349	Peter Randall Schunk	Org. 1815
4. MS1411	Ryan P. Haggerty	Org. 1816
5. MS9042	Scott T. Peterson	Org. 8343
6. MS9054	Sarah W. Allendorf	Org. 8350
7. MS9153	Timothy J. Shepodd	Org. 8220
8. MS9161	Norman C. Bartelt	Org. 8342
9. MS9161	Christian Mailhiot	Org. 8340
10. MS9161	Jonathan A. Zimmerman	Org. 8367
11. MS9402	Alfredo M. Morales	Org. 8126
12. MS9402	F. Patrick Doty	Org. 8126
13. MS9403	Michael E. Foster	Org. 8344
14. MS9403	Marie Kane	Org. 8344
15. MS9957	Reese E. Jones	Org. 8343
16. MS9957	Donald Ward	Org. 8126
17. MS9957	Xiaowang Zhou	Org. 8343
18. MS0899	Technical Library	Org. 9536 (electronic copy)
19. MS0359	D. Chavez, LDRD Office	Org. 1911
20. MS0161	Legal Technology Transfer Center	Org. 11500

7. REFERENCES

1 M. Shorohov, M. Kouznetsov, I. Lisitskiy, V. Ivanov, V. Gostilo, and A. Owens, IEEE Trans. Nucl. Sci., 56, 1855 (2009).
2 K. Hitomi, M. Matsumoto, O. Muroi, T. Shoji, and Y. Hiratate, IEEE Trans. Nucl. Sci., 49, 2526 (2002).
3 T. E. Schlesinger, J. E. Toney, H. Yoon, E. Y. Lee, B. A. Brunett, L. Franks, and R. B. James, Mater. Sci. Eng., R32, 103 (2001).
4 A. Churilov, G. Ciampi, H. Kim, L. Cirignano, W. Higgins, F. Olschner, and K. Shah, IEEE Trans. Nuc. Sci., 56, 1875 (2009).
5 M. Shorohov, M. Kouznetsov, I. Lisitskiy, V. Ivanov, V. Gostilo, and A. Owens, IEEE Trans. Nuc. Sci., 56, 1855 (2009).
6 K. Hitomi, Y. Kikuchi, T. Shoji, and K. Ishii, IEEE Trans. Nucl. Sci., 56, 1859 (2009).
7 K. Hitomi, T. Shoji, and Y. Nlizeki, Nuc. Instrum. Meth. Phys. Res. A, 585, 102 (2008).
8 V. Kozlov, M. Kemell, M. Vehkamaki, and M. Leskela, Nuc. Instrum. Meth. Phys. Res. A, 576, 10 (2007).
9 B. Dönmez, Z. He, H. Kim, L. Cirignano, and K. Shah, Nuc. Instru. Meth. Phys. Res. A, 623, 1024 (2010).
10 F. Costa, C. Mesquita, and M. Hamada, IEEE Trans. Nuc. Sci., 56, 1817 (2009).
11 A. Kozorezov, V. Gostilo, A. Owens, F. Quarati, M. Shorohov, M. A. Webb, and J. K. Wigmore, J. App. Phys., 108, 064507 (2010).
12 A. Datta, P. Becla, and S. Motakef, Nuc. Instrum. Meth. Phys. Res. A, 784, 37 (2015).
13 T. Onodera, K. Hitomi, and T. Shoji, IEEE Trans. Nuc. Sci., 54, 860 (2007).
14 T. Onodera, K. Hitomi, and T. Shoji, Nuc. Instru. Meth. A, Phys. Res. A, 576, 433 (2006).
15 I. B. Oliveira, F. E. Costa, P. K. Kiyohara, and M. M. Hamada, IEEE Trans. Nucl. Sci. 52, 2058 (2005).
16 A. M. Conway, L. F. Voss, A. J. Nelson, P. R. Beck, T. A. Laurence, R. T. Graff, R. J. Nikolic, S. A. Payne, H. Kim, L. J. Cirignano, and K. Shah, IEEE Trans. Nuc. Sci., 60, 1231 (2013).
17 V. Gostilo, A. Owens, M. Bavdaz, I. Lisjutin, A. Peacock, H. Sipila, and S. Zatoloka, IEEE Trans. Nucl. Sci. 49, 2513 (2002).
18 H. Kim, L. Cirignano, A. Churilov, G. Ciampi, W. Higgins, F. Olschner, and K. Shah, IEEE Trans. Nucl. Sci. 56, 819 (2009).
19 V. Lordi, J. Cryst. Growth, 379, 84 (2013).
20 C. R. Leaõ, and V. Lordi, Phys. Rev. Lett., 108, 246604 (2012).
21 C. R. Leaõ, and V. Lordi, Phys. Rev. B, 87, R081202 (2013).
22 X. W. Zhou, M. E. Foster, Reese Jones, P. Yang, H. Fan, and F. P. Doty, J. Mater. Sci. Res., 4, 15 (2015).
23 X. W. Zhou, M. E. Foster, P. Yang, and F. P. Doty, MRS Advances, doi: 10.1557/adv.2016.506.
24 S. Plimpton, J. Comput. Phys., 117, 1 (1995). lammps.sandia.gov.
25 J. X. M. Zheng-Johansson, and R. L. McGreevy, Solid State Ionics, 83, 35 (1996).

26 J. X. M. Zheng-Johansson, I. Ebbsjo, and R. L. McGreevy, Solid State Ionics, 82, 115 (1995).
27 C. W. Huang, W. C. J. Wei, C. S. Chen, and J. C. Chen, J. Euro. Cer. Soc., 31, 3159 (2011).
28 K.-L. Tung, K.-S. Chang, C.-C. Hsiung, Y.-C. Chiang, and Y.-L. Li, Separation Purification Tech., 73, 13 (2010).
29 Y. Yamamura, S. Kawasaki, and H. Sakai, Solid State Ionics, 126, 181 (1999).
30 R. W. J. M. Huang Foen Chung, and S. W. de Leeuw, Solid State Ionics, 175, 851 (2004).
31 J. V. L. Beckers, K. J. van der Bent, and S. W. de Leeuw, Solid State Ionics, 133, 217 (2000).
32 P. J. D. Lindan, and M. J. Gillan, J. Phys.: Condens. Matter, 5, 1019 (1993).
33 D. Marrocchelli, P. A. Madden, S. T. Norberg, and S. Hull, Chem. Mater., 23, 1365 (2011).
34 F. H. Stillinger and T. A. Weber, Phys. Rev. B 31, 5262 (1985).
35 X. W. Zhou, D. K. Ward, J. E. Martin, F. B. van Swol, J. L. Cruz-Campa, and D. Zubia, Phys. Rev. B, 88, 085309 (2013).
36 X. W. Zhou, R. E. Jones, C. J. Kimmer, J. C. Duda, and P. E. Hopkins, Phys. Rev. B, 87, 094303 (2013).
37 X. W. Zhou, R. E. Jones, J. C. Duda, and P. E. Hopkins, Phys. Chem. Chem. Phys., 15, 11078 (2013).
38 X. W. Zhou, M. E. Foster, F. B. van Swol, J. E. Martin, and B. M. Wong, J. Phys. Chem. C, 118, 20661 (2014).
39 J. Wang, and A. Rockett, Phys. Rev. B 43, 12571 (1991).
40 J. Tersoff, Phys. Rev. B 39, 5566 (1989).
41 K. Albe, K. Nordlund, J. Nord, and A. Kuronen, Phys. Rev. B 66, 035205 (2002).
42 X. W. Zhou, and R. E. Jones, Modelling Simul. Mater. Sci. Eng., 19, 025004 (2011).
43 M. S. Daw, and M. I. Baskes, Phys. Rev. B, 29, 6443 (1984).
44 D. G. Pettifor, M. W. Finnis, D. Nguyen-Manh, D. A. Murdick, X. W. Zhou, and H. N. G. Wadley, Mater. Sci. Eng. A, 365, 2 (2004).
45 J. D. H. Donnay, and H. M. Ondik, “crystal data, determinative tables”, 3rd ed., Vol. 2 (inorganic compounds), U. S. Department of Commerce, National Bureau of Standards, and Joint Committee on Power Diffraction Standards, U. S. A., 1973.
46 I. Barin, “thermochemical data of pure substances”, VCH, Weinheim, 1993.
47 G. Simmons, “single crystal elastic constants and calculated aggregate properties”, Southern Methodist University Press, 1965.
48 G. E. Morse, and A. W. Lawson, J. Phys. Chem. Solids, 28, 939 (1967).
49 S. Wolfram, The Mathematica Book, 5th ed. (Wolfram Research, Inc., Champaign, IL, 2004), p. 106ff.
50 M. R. Hestenes, and E. Stiefel, J. Res. National Bureau Stand., 49, 409 (1952).
51 D. M. Olsson, and L. S. Nelson, Technometrics, 17, 45 (1975).
52 R. Storn, and K. Price, J. Global Opt., 11, 341 (1997).
53 S. Kirkpatrick, C. D. Gelatt, and M. P. Vecchi, Science, 220, 671 (1983).
54 D. K. Ward, X. W. Zhou, B. M. Wong, F. P. Doty, and J. A. Zimmerman, Phys. Rev. B, 86, 245203 (2012).
55 D. K. Ward, X. W. Zhou, B. M. Wong, F. P. Doty, and J. A. Zimmerman, Phys. Rev. B, 85, 115206 (2012).

56 D. K. Ward, X. W. Zhou, B. M. Wong, and F. P. Doty, J. Mol. Modell., 19, 5469 (2013).
57 Y. P. Afinogenov, and T. N. Larionova, Russ. J. Inorg. Chem., 37, 1344 (1992).
58 H. Kim, A. Churilov, G. Ciampi, L. Cirignano, W. Higgins, S. Kim, P. O'Dougherty, F. Olschner, and Kanai Shah, Nucl. Instrum. Meth. Phys. Res. A, 629, 192 (2011).
59 S. B. Zhang, and J. E. Northrup, Phys. Rev. Lett., 67, 2339 (1991).
60 J. E. Northrup, and S. B. Zhang, Phys. Rev. B, 47, 6791 (1993).
61 J. Klimeš, D. R. Bowler, and A. Michaelides, Phys. Rev. B, 83, 195131 (2011).
62 J. Heyd, G. E. Scuseria, and M. Ernzerhof, J. Chem. Phys., 118, 8207 (2003).
63 S. Grimme, J. Comp. Chem., 27, 1787 (2006).
64 G. Kresse, and J. Hafner, Phys. Rev. B, 47, 558 (1993).
65 G. Kresse, and J. Hafner, Phys. Rev. B, 49, 14251 (1994).
66 G. Kresse, and J. Furthmüller, Comp. Mater. Sci., 6, 15 (1996).
67 G. Kresse, and J. Furthmüller, Phys. Rev. B, 54, 1169 (1996).
68 L. Pauling, J. Am. Chem. Soc. 54, 3570 (1932).
69 R. S. Mulliken, J. Chem. Phys. 2, 782 (1934).
70 F. H. Streitz and J. W. Mintmire, Phys. Rev. B 50, 11996 (1994).
71 X. W. Zhou, H. N. G. Wadley, J.-S. Filhol, and M. N. Neurock, Phys. Rev. B 69, 035402 (2004).
72 X. Gonze, and C. Lee, Phys. Rev. B, 55, 10355 (1997).
73 A. Stukowski, Modelling Simul. Mater. Sci. Eng., 18, 015012 (2010). http://www.ovito.org/.
74 R. A. Robinson, R. H. Stokes, "Electrolyte Solutions" (Academic Press, Inc., New York, 1995).
75 Ç. Tasseven, O. Alcaraz, J. Trullàs, M. Silbert, and A. Giró, J. Phys.: Condens. Matter, 9, 11061 (1997).
76 X. W. Zhou, M. E. Foster, P. Yang, and F. P. Doty, to be submitted.
77 R. Hofstadter, Phys. Rev., 72, 1120 (1947).
78 K. Hitomi, T. Murayama, T. Shoji, T. Suehiro, and Y. Hiratate, Nucl. Instrum. Methods Phys. Res. A, 428, 372 (1999).
79 K. Hitomi, O. Muroi, M. Matsumoto, R. Hirabuki, T. Shoji, T. Suehiro, and Y. Hiratate, Nucl. Instrum. Methods Phys. Res. A, 458, 365 (2001).
80 K. Hitomi, T. Onodera, and T. Shoji, Nucl. Instrum. Methods Phys. Res. A, 579, 153 (2007).
81 V. Kozlov, H. Andersson, V. Gostilo, M. Leskela, A. Owens, M. Shorohov, and H. Sipila, Nucl. Instrum. Methods Phys. Res. A, 591, 209 (2008).
82 V. Kozlov, M. Leskela, and H. Sipila, Nucl. Instrum. Methods Phys. Res. A, 546, 200 (2005).
83 V. Kozlov, M. Leskela, M. Vehkama, and H. Sipila, Nucl. Instrum. Methods Phys. Res. A, 573, 212 (2007).
84 V. Kozlov, M. Leskela, M. Kemell, and H. Sipila, Nucl. Instrum. Methods Phys. Res. A, 563, 58 (2006).
85 I. B. Oliveira, F. E. da Costa, J. F. D. Chubaci, and M. M. Hamada, IEEE Trans. Nucl. Sci., 51, 1224 (2004).
86 I. B. Oliveira, J. F. D. Chubaci, M. J. A. Armelin, and M. M. Hamada, Cryst. Res. Technol., 39, 849 (2004).